Pergamon

Computers Math. Applic. Vol. 34, No. 9, pp. 95–121, 1997

0898-1221/97 $17.00 + 0.00

PII: S0898-1221(97)00192-2

De Triangularitate Quadranguli or Symmetry Regions and Symmetry Centroids of Geometric Figures

A. E. KÖHLER
Lehrstuhl Biophysik, Institut für Biochemie und Biophysik
Friedrich-Schiller-Universität Jena
Philosophenweg 12, D-07743 Jena, Germany
koehler@merlin.biologie.uni-jena.de

Dedicated to Professor Dr. Eberhard Müller on the occasion of his 65th birthday.

(Received October 1996; accepted December 1996)

Abstract—The fuzzy symmetry concept allows, for plane geometric figures, a separate characterisation of the degrees of $\mathbf{C}_n$ symmetry (polymetry) and $\mathbf{C}_{nv}$ symmetry (polysymmetry). A new method for the evaluation of these degrees of symmetry δ from the areas of the maximal $\mathbf{C}_n$ and $\mathbf{C}_{nv}$ regions within a figure is presented. Since δ depends on the rotation point position, *symmetry profiles* and *symmetry landscapes* of a figure can be calculated which give a detailed local characterisation of the figure with respect to arbitrary symmetries. From such landscapes, *symmetry centroids* of a figure are determined. It is shown that the different symmetry centroids do not coincide in figures with low symmetry ($\mathbf{C}_1$, $\mathbf{C}_{1v}$).

Keywords—Fuzzy symmetry, Degree of symmetry, Orbit, Symmetry centroid, Symmetry landscape, Poly(sym)metry.

1. INTRODUCTION

A fuzzy symmetry concept for plane geometric figures $\mathcal{F}$, based on a Fourier analysis of the figure's contour function $R(\varphi)$ (R: radius, φ: azimuthal angle)

$$R(\varphi) = \sum_{k=0}^{\infty} a_k \cos k\varphi + \sum_{k=1}^{\infty} b_k \sin k\varphi = \sum_{k=0}^{\infty} c_k \cos(k\varphi - \varphi_k) \equiv \sum_{k=0}^{\infty} c_k F_k \tag{1.1}$$

has been developed in [1]. The central notion of this concept is the *degree of symmetry* $\delta(\mathbf{G})$ of a figure with respect to a certain symmetry $\mathbf{G}$. It can be evaluated for arbitrary symmetry groups $\mathbf{G}$, so that the crisp characterisation of a figure by its symmetry group $\mathbf{G}_A$[1] will be replaced by a *symmetry vector*[2]

[1]This symmetry group has been named "actual symmetry" in [1].

[2]There are only two types of two-dimensional point groups, $\mathbf{C}_n$ and $\mathbf{C}_{nv}$. Here, $\mathbf{C}_n$ denotes a rotation group (cyclic group) having only an n-fold rotation point; $\mathbf{C}_{nv}$ denotes a group consisting of an n-fold rotation point and n mirror lines. We use the Schoenflies-Niggli nomenclature; the corresponding international (Hermann-Mauguin) symbols are n for $\mathbf{C}_n$, nm for $\mathbf{C}_{nv}$ (n odd), and nmm for $\mathbf{C}_{nv}$ (n even) [2,3]. Since there is no canonical Schoenflies notation for two-dimensional groups [4, p. 753], we use for the latter type of groups the symbol "$\mathbf{C}_{nv}$" and at the same time abandon the nomenclature of Klemm [2] ("$\mathbf{D}_n$"), since these groups are direct analogues of the three-dimensional $\mathbf{C}_{nv}$ groups, whereas they are only *isomorphous* to the three-dimensional dihedral groups $\mathbf{D}_n$. The symbol C_n denotes an n-fold rotation point, n is called the *multiplicity* of this point.

$$\vec{\delta}(\mathcal{F}) = (\delta(\mathbf{C}_1), \delta(\mathbf{C}_{1v}), \ldots, \delta(\mathbf{C}_\infty), \delta(\mathbf{C}_{\infty v}))\,, \tag{1.2}$$

which can also be visualised by a *symmetry spectrum* for the figure.

As can be seen from $\vec{\delta}(\mathcal{F})$, the fuzzy symmetry analysis gives degrees of symmetry *separately* for $\mathbf{C}_n$ and $\mathbf{C}_{nv}$ groups. Following the crystallographer Tschermak [5], these two different symmetry types can be given their own designations. Crystal faces displaying only $\mathbf{C}_n$ rotation symmetry have been named monometric (asymmetric), dimetric, trimetric, etc., for $n = 1, 2, 3$, whereas faces with $\mathbf{C}_{nv}$ symmetry have been termed monosymmetric, disymmetric, trisymmetric, etc. We will complete this nomenclature by introducing the term *"circularity"* for the (degree of) $\mathbf{C}_{\infty v}$ symmetry and the generic terms *"polymetry"* and *"polysymmetry"* (cf., Section 3).

In the following, a plane geometric figure $\mathcal{F}$ will be regarded as a *region* of Euclidean space ($\mathcal{F} \subset \mathbb{R}^2$). In this case, the degree of symmetry with respect to a symmetry group $\mathbf{G} = \{G_k \mid k=1,\ldots,g\}$ of order g has been evaluated in [6] from the degree of overlap of the original figure $\mathcal{F}$ and the transformed figure $\mathcal{F}' = G \cdot \mathcal{F}$ for groups $\mathbf{G} = \{E, G\}$ of order 2 ($\mathbf{C}_2$, $\mathbf{C}_{1v}$):

$$\delta(\mathbf{G}) = \frac{A(\mathcal{F} \cap \mathcal{F}')}{A(\mathcal{F})} \tag{1.3}$$

(E: identity element, A: area). This concept will be extended to arbitrary groups in the following. The method presented here for the evaluation of $\delta(\mathbf{G})$ is based on the concept of orbits of points (Section 2.2), but it is equivalent to a construction of the overlap area and an extension of equation (1.3).

The results of this method show that unusual fuzzy symmetries, e.g., a threefold symmetry in a square, are due to the existence of regions within the square which objectively display threefold symmetry. On this basis, the concept of a *symmetry centroid* will be developed. Then, we show that the different symmetry centroids of a geometric figure $\mathcal{F}$, which in the case of a higher symmetry of $\mathcal{F}$, coincide with its barycentre (centre of gravity, centroid), in the case of low symmetry ($\mathbf{C}_1$, $\mathbf{C}_{1v}$) of $\mathcal{F}$ will fall apart.

2. RESULTS

2.1. The Triangularity of the Square

In [1], the existence of *arbitrary* symmetries within a given figure $\mathcal{F}$ has not been discussed in detail, but left to a later paper. But the data presented there (in Figure 1, the Fourier spectra for a square and a rectangle are displayed together with their symmetry spectra derived from the data of [1] with the method used there[3]) show that, astonishingly, in a square, we find a relatively large number of symmetries one will normally not associate with such a figure: $\mathbf{C}_{3v}$, $\mathbf{C}_{5v}$, $\mathbf{C}_{6v}$, $\mathbf{C}_{7v}$, and others (Figure 1c).

We will discuss here, as an example, the degree of threefold symmetry. It results from two contributions.

- First, the Fourier term F_0 corresponds to a *circle* having $\mathbf{C}_{\infty v}$ symmetry. Thus, it contributes to the degrees of symmetry for *every* group $\mathbf{G}$ ($\mathbf{G}$ being a subgroup of $\mathbf{C}_{\infty v}$). Therefore, no degree of symmetry can be lower than the relative contribution of F_0 to the Fourier spectrum of the figure.
- Second, in principle, all Fourier terms F_k with $k \equiv 0 (\mathrm{mod}\, 3)$ contribute to $\delta(\mathbf{C}_3)$ or $\delta(\mathbf{C}_{3v})$ [1]. Since, on the other hand, the square actually has a crisp *fourfold* symmetry,

[3]The degrees of symmetry have been evaluated from the Fourier spectrum by a symmetry check algorithm which checks all Fourier terms for compatibility with all $\mathbf{C}_n$ and $\mathbf{C}_{nv}$ symmetries for $n = 1, \ldots, 12$. The algorithm takes every term which is compatible with the tested symmetry as reference term and checks all other terms for a maximum degree of correspondence (see [1]).

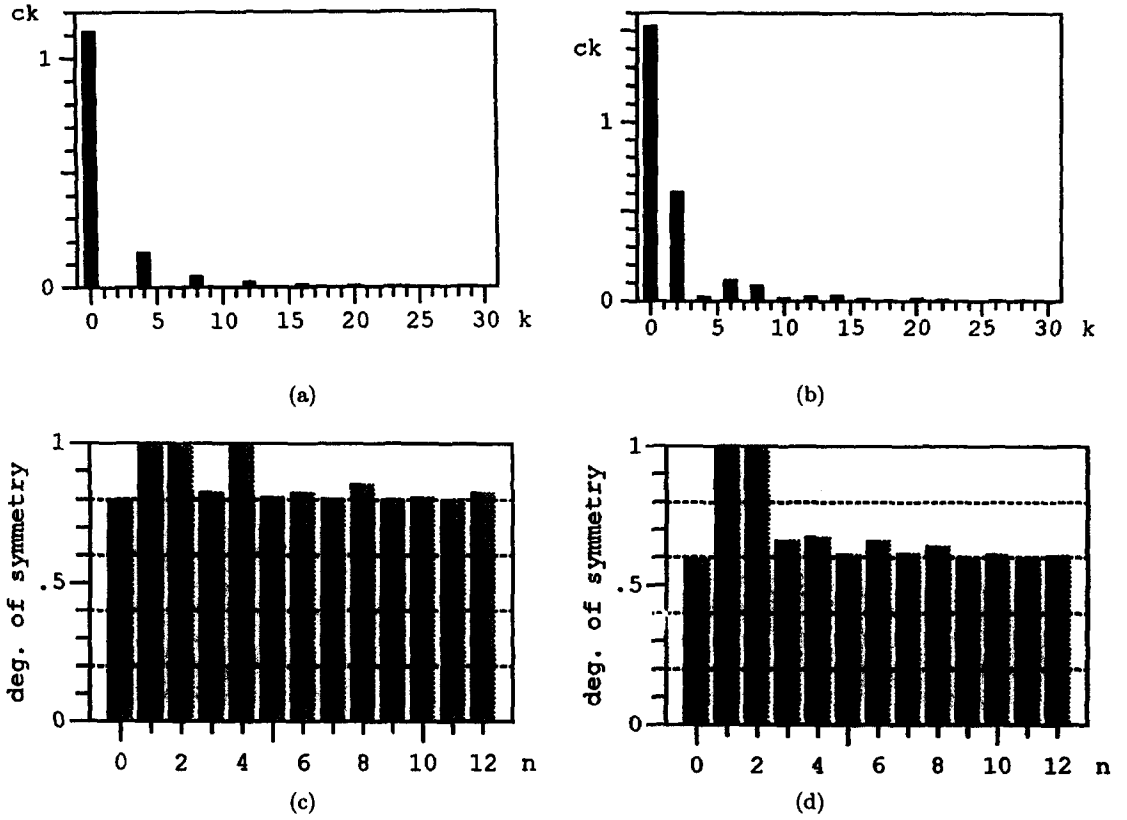

Figure 1. Fourier spectra $c_k = f(k)$ (a),(b) and the corresponding symmetry spectra (c),(d) for a square (a),(c) and a rectangle with side ratio $b/a = 2$ (b),(d). The degrees of symmetry have been evaluated using the method described in [1]. In the symmetry spectra, filled bars correspond to $\mathbf{C}_{nv}$ groups and dotted bars to $\mathbf{C}_n$ groups (for both figures, we have $\delta(\mathbf{C}_{nv}) = \delta(\mathbf{C}_n)$ for all values of n); $\delta(\mathbf{C}_\infty)$ and $\delta(\mathbf{C}_{\infty v})$ have been plotted at the position $n = 0$.

all Fourier terms disturbing this symmetry must vanish [1]. Therefore, contributions to $\delta(\mathbf{C}_3)$ or $\delta(\mathbf{C}_{3v})$ can come only from the Fourier terms $F_{3 \cdot 4 \cdot m}$ with $m = 1, 2, \ldots$, as far as they are present in the Fourier spectrum of the square. Indeed, the Fourier spectrum (Figure 1a) shows that the F_{12} term is present with a distinct weight, whereas the term F_3 is absent.

For a rectangle (Figures 1b and 1d) or arbitrary other figures, the discussion is analogous. In sum, the Fourier spectrum of a figure $\mathcal{F}$ having the crisp symmetry $\mathbf{G}_A$ contains only terms which are *compatible* with $\mathbf{G}_A$. This compatibility condition is fulfilled for all Fourier terms whose symmetries correspond to *supergroups* $\mathbf{G}_A^+$ of $\mathbf{G}_A$ [1].[4] On the other hand, trivially, if a figure $\mathcal{F}$ has the crisp symmetry $\mathbf{G}_A$, then the degree of symmetry equals unity for $\mathbf{G}_A$, and likewise, for all groups $\mathbf{G}_A^-$ which are *subgroups* of $\mathbf{G}_A$. This means, however, that if a Fourier term corresponding to a supergroup $\mathbf{G}_A^+$ of $\mathbf{G}_A$ is present, it contributes to all symmetries $\mathbf{G}_A^\mp$ which are subgroups of this supergroup. Some of these $\mathbf{G}_A^\mp$ groups are also subgroups or supergroups of $\mathbf{G}_A$, but others (denoted by $\mathbf{G}_A^\neq$) are not. The existence of the latter groups is the deeper reason for the finding that in a square there exist "strange" symmetries ($\mathbf{C}_{nv}$ with $n = 3, 5, 6, 7$, and so on), which *per se* are not compatible with the actual symmetry of the square ($\mathbf{C}_{4v}$). The relations between the different symmetry groups for $\mathbf{G}_A = \mathbf{C}_{4v}$ are depicted in Figure 2.

In the following, we present a new method for the evaluation of degrees of symmetry which immediately shows the regions of arbitrary symmetries in a geometric figure.

[4]This statement is always true for rotation groups $\mathbf{C}_n$. For the compatibility of $\mathbf{C}_{nv}$ groups, the angular orientation of their sets of mirror lines will become crucial, as is outlined in [1].

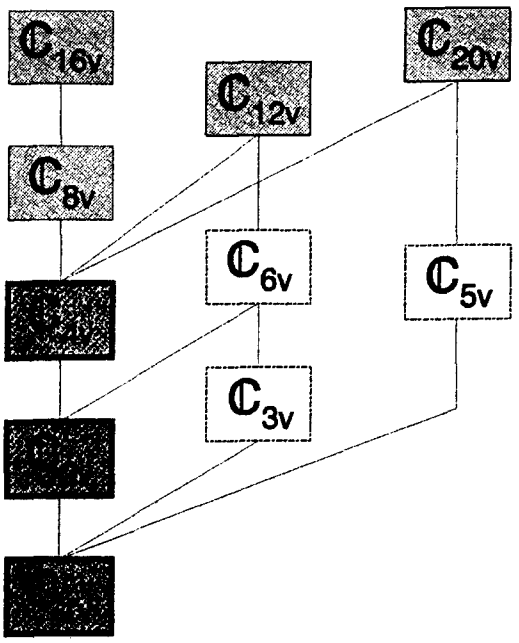

Figure 2. Symmetry relationships for the square, illustrated by a part of the pedigree of symmetry groups centering around the actual symmetry $\mathbf{G}_A = \mathbf{C}_{4v}$. Dark boxes: $\mathbf{G}_A$ and its subgroups, for which $\delta(\mathbf{G}) = 1$; dotted boxes: compatible supergroup symmetries $\mathbf{G}_A^+$; open boxes: subgroups $\mathbf{G}_A^{\neq}$ of these supergroups (see text). Lines connect a group with its maximal subgroups.

2.2. Orbits of Points and Symmetry Regions in a Geometric Figure

The notion of an *orbit* stems from crystallography [4, p. 724f] and will be defined for our purposes as follows.

DEFINITION. *The set of all points that are symmetrically equivalent to a point P with respect to a group $\mathbf{G}$ is called the orbit $\Omega(P, \mathbf{G})$ of P with respect to $\mathbf{G}$. Then, $\Omega(P, \mathbf{G})$ is the set of images of P under the operations of $\mathbf{G}$ (cf., [4, p. 724f]).*

The fact that the orbit of a certain point P depends on the position of the rotation point $Z = C_n$ of $\mathbf{G}$ will (if necessary) be indicated by writing $\Omega(P, \mathbf{G}, Z)$. Orbits for $\mathbf{C}_{nv}$ groups are not unique unless the orientation angle ε (with $0 \leq \varepsilon < (\pi/n)$) of the set of mirror lines is specified so that we should write $\Omega(P, \mathbf{C}_{nv}, Z, \varepsilon)$ in this case.

To the above definition, we will add the notion of a $\mathbf{G}$-*symmetry region* $\mathcal{G}(\mathbf{G}, Z)$ of a geometric figure.

DEFINITION. *The $\mathbf{G}$-symmetry region $\mathcal{G}(\mathbf{G}, Z)$ of a figure $\mathcal{F}$ is the set of all points P whose orbits $\Omega(P, \mathbf{G}, Z)$ with respect to $\mathbf{G}$ and a given position of the rotation point Z lie entirely within $\mathcal{F}$:*

$$\mathcal{G}(\mathbf{G}, Z) = \{P \mid \Omega(P, \mathbf{G}, Z) \in \mathcal{F}\}. \tag{2.1}$$

If the dependence of $\mathcal{G}(\mathbf{G}, Z)$ on the position of the rotation point needs not to be stressed, the symbol "Z" will be omitted. On the other hand, for $\mathbf{C}_{nv}$ groups, we shall also write $\mathcal{G}(\mathbf{C}_{nv}, Z, \varepsilon)$ as for orbits.

An orbit $\Omega(P, \mathbf{C}_n)$ generally consists of $g = n$ points[5] and may be subdivided into n/d disjunct suborbits $\Omega_j(P^{(j)}, \mathbf{C}_d)$ with $j = 1, \ldots, n/d$ whose multiplicity d is a divisor of n. The symmetry

[5]For points in special positions (on symmetry elements of $\mathbf{G}$), the number of points in the orbit is reduced (down to one for a point lying in Z), but the results that follow can be transferred to this case if, for instance, g/g^- is replaced by g_Ω/g_Ω^-, the orders of the orbits corresponding to $\mathbf{G}$ and $\mathbf{G}^-$ for that special position.

of each suborbit is $\mathbf{C}_d$. This can be shown by a rearrangement of the elements of $\mathbf{C}_n$ (exemplified for $\mathbf{C}_6$) and using the fact that there is a one-to-one correspondence between the points of an orbit and the symmetry operations of $\mathbf{G}$ [4, p. 724f],

$$\begin{aligned}\mathbf{C}_6 &= \{E, C_6, C_6^2, C_6^3, C_6^4, C_6^5, \} \\ &= \{E, C_6^2 \equiv C_3, C_6^4 \equiv C_3^2 \mid C_6 \cdot E, C_6^3 \equiv C_6 C_3, C_6^5 \equiv C_6 C_3^2\} \\ &= \{E, C_6^3 \equiv C_2 \mid C_6 \cdot E, C_6^4 \equiv C_6 C_2 \mid C_6^2 \cdot E, C_6^5 \equiv C_6^2 C_2\}.\end{aligned} \tag{2.2}$$

This example shows that an orbit $\Omega(P, \mathbf{C}_6)$ can be decomposed into two suborbits à three points which are transformed into one another by $\mathbf{C}_3$ or into three suborbits à two points, each subset with $\mathbf{C}_2$ symmetry. Therefore, we have

$$\Omega(P, \mathbf{C}_n) = \bigcup_{j=1}^{n/d} \Omega_j \left(P^{(j)}, \mathbf{C}_d\right), \qquad \text{for } n \equiv 0 \pmod d, \tag{2.3}$$

where $P^{(j)} = C_n^{j-1} \cdot P$. Furthermore, we conclude that

$$\Omega(P, \mathbf{C}_n) \in \mathcal{F} \Longrightarrow \Omega_j \left(P^{(j)}, \mathbf{C}_d\right) \in \mathcal{F}, \qquad j = 1, \ldots, \frac{n}{d}, \tag{2.4}$$

i.e., *if* $\Omega(P, \mathbf{C}_n)$ lies in $\mathcal{F}$, then it must be contained in $\mathcal{G}(\mathbf{C}_d)$, since all its d-fold disjunct suborbits lie in $\mathcal{F}$ and, therefore, also in $\mathcal{G}(\mathbf{C}_d)$. In other words,

$$\mathcal{G}(\mathbf{C}_n) \subseteq \mathcal{G}(\mathbf{C}_d), \qquad \text{for } n \equiv 0 \pmod d. \tag{2.5}$$

This result can be generalised to $\mathbf{C}_{nv}$ groups. The corresponding orbits may be regarded as consisting of two suborbits which result from a rearrangement of $\mathbf{C}_{nv}$ analogous to that of $\mathbf{C}_n$ above:

$$\Omega(P, \mathbf{C}_{nv}) = \Omega(P, \mathbf{C}_n) \bigcup \Omega(\sigma \cdot P, \mathbf{C}_n) \tag{2.6}$$

(σ: any of the mirror lines of $\mathbf{C}_{nv}$). Summarising, we find that $\Omega(P, \mathbf{G})$ will, for every possible subgroup $\mathbf{G}^-$ of $\mathbf{G}$, contain g/g^- disjunct suborbits, all having the symmetry $\mathbf{G}^-$. Therefore, a symmetry region $\mathcal{G}(\mathbf{G})$ must include all orbits having the symmetry $\mathbf{G}$ or some if its supergroups $\mathbf{G}^+$ if they lie in $\mathcal{F}$:

$$\mathcal{G}\left(\mathbf{G}^+\right) \subseteq \mathcal{G}(\mathbf{G}), \qquad \text{for } \mathbf{G}^+ \supset \mathbf{G}. \tag{2.7}$$

There exists a simple construction algorithm for the polymetry region of a figure $\mathcal{F}$ (see Figure 3). The contour of $\mathcal{F}$ is rotated n times through $2\pi k/n$ ($k = 0, \ldots, n-1$) about the rotation point $Z = C_n$. If $\mathcal{F}$ is polygonal and convex,[6] there results an *inner polygon* around Z which is exactly the polymetry region being sought.[7] For concave figures $\mathcal{F}$ and rotation point positions *outside* $\mathcal{F}$, the polymetry region may consist of nonconnected polygons (see Figure 3c). Transformation of $\mathcal{F}$ by an additional set of n reflections gives the *polysymmetry* region of $\mathcal{F}$. In this case, the orientation angle ε of the set of mirror lines must be specified. In any case, we have

$$\mathcal{G}(\mathbf{G}) = \bigcap_{k=1}^{g} \mathcal{F}^{(k)}, \qquad \text{where } \mathcal{F}^{(k)} = G_k \cdot \mathcal{F}, \tag{2.8}$$

[6] A polygonal figure $\mathcal{F}$ is termed convex if it is situated on only one side of any line containing some side of the polygon (a convex figure has no re-entrant angles). Otherwise, it is called concave [7, Volume 7, p. 221; 8].

[7] An analogous procedure can be performed with the contour function $R(\varphi)$ of the figure by comparing the $R(\varphi + 2\pi k/n)$ values for $k = 0, \ldots, n-1$ and building a new contour function $R_n(\varphi)$ by taking the *minimum* value from the above set of radii for each angle φ. Then, $R_n(\varphi)$ necessarily has an n-fold rotation symmetry and represents the contour function of the polymetry region of $\mathcal{F}$.

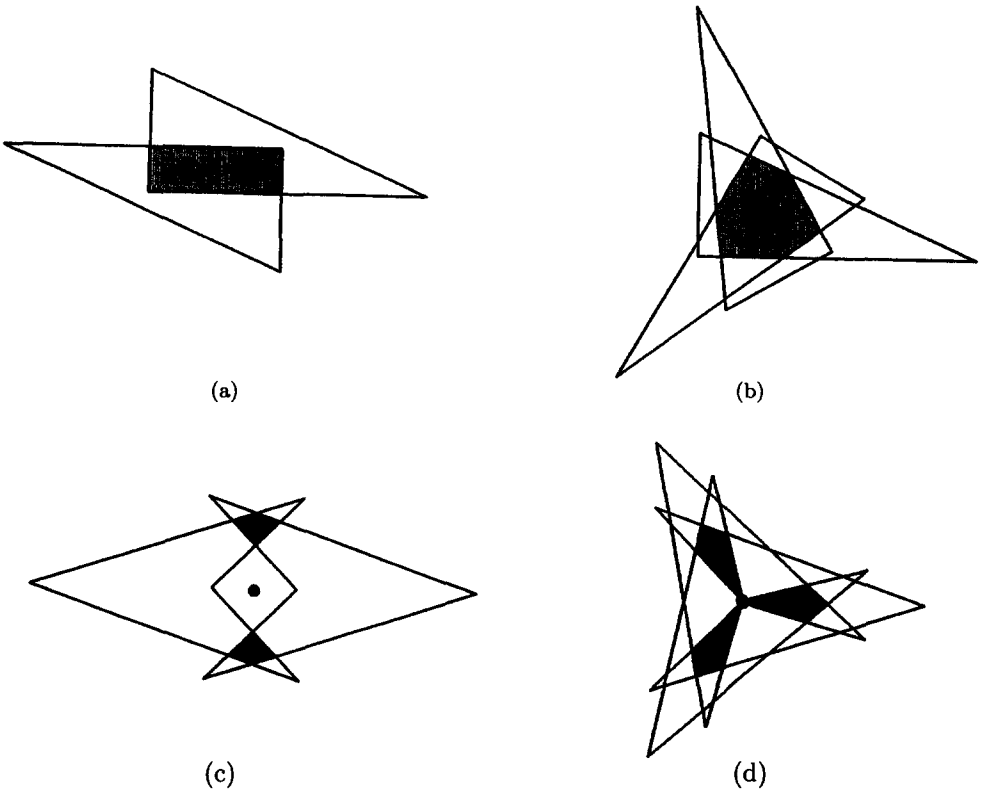

Figure 3. Construction of the dimetry (a),(c) and trimetry (b),(d) regions for a right triangle (a),(b) and an arrowhead figure (c),(d) (see text). The positions of the rotation points Z are indicated. For the concave arrowhead figure, symmetry regions are shown for positions of the rotation point outside (c) and inside (d) the figure.

where the G_k are the symmetry operations of $\mathbf{G}$, and $\mathcal{F}^{(k)}$ the corresponding transformed figures. Here, the figure $\mathcal{F}^{(k)}$ comprises the images of all points of $\mathcal{F}$ under the symmetry operation G_k of $\mathbf{G}$. Therefore, the *union* $\cup_k \mathcal{F}^{(k)}$ contains all orbits of the points of $\mathcal{F}$ with respect to $\mathbf{G}$. In contrast, the *intersection* $\cap_k \mathcal{F}^{(k)}$ contains only those orbits which lie entirely within $\mathcal{F}$, so that this construction algorithm for $\mathcal{G}(\mathbf{G})$ is equivalent to the definition of $\mathcal{G}(\mathbf{G})$ using orbits of points (*vide supra*). Figure 3 illustrates the constructions for the dimetry and trimetry regions of a right triangle and an arrowhead figure as examples.

In sum, the $\mathbf{G}$-symmetry region $\mathcal{G}(\mathbf{G})$ of $\mathcal{F}$ corresponds to the part ($\mathcal{G}(\mathbf{G}) \subseteq \mathcal{F}$) of $\mathcal{F}$ which displays *at least* symmetry $\mathbf{G}$ (strictly speaking, $\mathbf{G}$ or one of its supergroups $\mathbf{G}^+$). It is the maximum region having symmetry $\mathbf{G}$ (with given rotation point $Z = C_n$) which can be drawn within $\mathcal{F}$.

The *area* A of a symmetry region $\mathcal{G}(\mathbf{G})$ will be used to define the corresponding *degree of symmetry* $\delta(\mathbf{G})$ as follows:

$$\delta(\mathbf{G}) = \frac{A(\mathcal{G}(\mathbf{G}))}{A(\mathcal{F})}, \tag{2.9}$$

i.e., the degree of symmetry is given by the relative contribution of the $\mathbf{G}$-symmetry region to the area of the whole figure $\mathcal{F}$.

2.3. $\mathbf{C}_n$-Symmetry (Polymetry) Regions of a Figure

The determination of the polymetry regions within a figure $\mathcal{F}$ has been done in the following, mainly with *discretized* figures. A polygonal figure is produced on the computer screen by filling its contour polygon. The rotation point $Z = C_n$ is then put on a certain discrete position (pixel), and all pixels of the figure are tested to see whether their orbits $\Omega(P, \mathbf{C}_n, Z)$ lie entirely within

Table 1. The geometric figures discussed in this paper and their vertex coordinates (integer pixel coordinates).

Figure	Pixel Coordinates
Square	$\mathcal{S}q = ((0,0),(200,0),(200,200),(0,200))$
Rectangle	$\mathcal{R}e = ((0,0),(400,0),(400,200),(0,200))$
Quadrangle 1	$\mathcal{Q}u1 = ((0,0),(200,0),(50,150),(0,100))$
Quadrangle 2	$\mathcal{Q}u2 = ((0,0),(200,0),(100,160),(0,120))$
Arrowhead figure	$\mathcal{A}r = ((0,0),(-100,-100),(200,0),(-100,100))$
Deltoid	$\mathcal{D}e = ((0,0),(100,-100),(300,0),(100,100))$
Parallelogram	$\mathcal{P}a = ((0,0),(200,0),(300,100),(100,100)$
Quadrangle, circumscr.	$\mathcal{Q}c = ((0,0),(400,0),(133.\bar{3},200),(0,200))$
Triangle, right	$\mathcal{T}r1 = ((0,0),(200,0),(0,120))$
Triangle, right	$\mathcal{T}r2 = ((0,0),(405,0),(0,300))$
Triangle, obtuse	$\mathcal{T}o = ((0,0),(200,0),(-20,120))$
Triangle, isosc. obtuse	$\mathcal{T}io = ((0,-100),(120,0),(0,100))$
Triangle, isosc. acute	$\mathcal{T}ia = ((0,-100),(240,0),(0,100))$
Pentagon, concave	$\mathcal{P}v = ((0,0),(200,0),(260,220),(0,200),(100,100))$
Swallowtail figure	$\mathcal{S}w = ((0,0),(120,110),(240,0),(240,240),(120,130),(0,240))$
Hexagon, concave	$\mathcal{H}v = ((0,0),(360,0),(260,180),(160,20),(160,160),(0,160))$
Hexagon, irregular	$\mathcal{H}i = ((0,0),(200,0),(260,100),(260,260),(60,260),(0,240))$
Octagon "8"	$\mathcal{O}e = ((0,0),(150,-150),(200,-100),(250,-150),$ $(400,0),(250,150),(200,100),(150,150))$
Octagon "pliers"	$\mathcal{O}p = ((0,0),(-100,-100),(-150,-50),(-100,-150),$ $(200,0),(-100,150),(-150,50),(-100,100))$

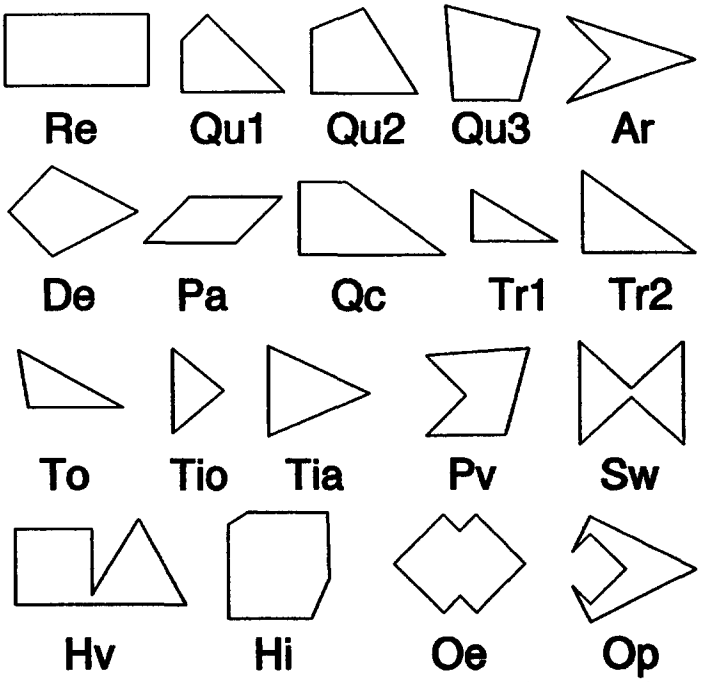

Figure 4. Sketches of the figures $\mathcal{F}$ discussed in this paper (not to scale). For the names of the figures, see Table 1.

the figure. The results are approximate, but for large figures, the error can be made sufficiently small, as can be seen from a comparison of the barycentre coordinates in Table 2 (relative errors were always below 0.5%). In contrast, C_∞-symmetry regions have been calculated with the *Mathematica* program [9] (in this case, the discrete method is too inaccurate). Since there exist

no simple planar figures having only $\mathbf{C}_\infty$ symmetry, the test for $\mathbf{C}_\infty$ symmetry always results in a solid *maximal circle* about Z whose radius is the minimum of all distances between Z and the sides of $\mathcal{F}$. This circle has $\mathbf{C}_{\infty v}$ symmetry, so that for arbitrary figures, we get $\delta(\mathbf{C}_\infty) = \delta(\mathbf{C}_{\infty v})$. Therefore, we have to speak about *circularity* here despite the fact that this chapter is dedicated to $\mathbf{C}_n$-symmetry regions.

In order to simplify the reference to the various figures discussed in this paper, all these figures are listed in Table 1 with the coordinates of their vertices. To give an impression of their shapes, they are sketched in Figure 4.

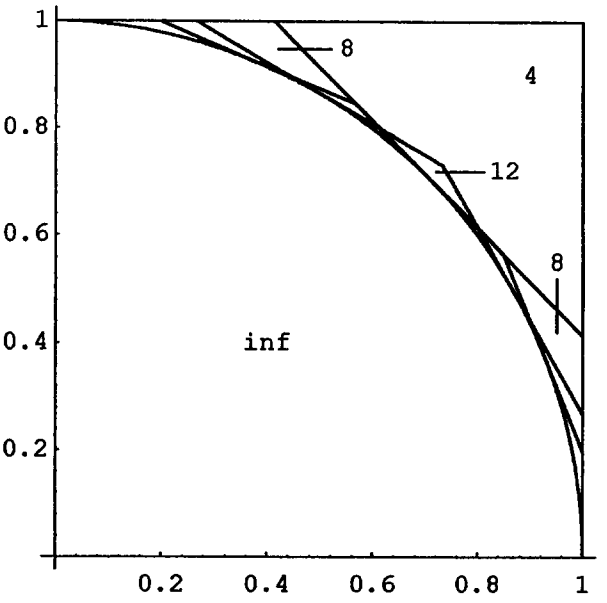

Figure 5. Regular $(4 \cdot k)$-gons ($k = 2, \ldots, \infty$) drawn within a square (only the positive quadrant is shown). Their superposition illustrates the regions $\mathcal{G}(n_{\max})$ of points with equal multiplicity $n_{\max}$ of their maximal orbits (see text). For some regions, these multiplicities are indicated ("inf" = ∞).

Examples of polymetry regions within different figures are given in Figures 6, 8, 10, and 11. These figures show the following.

(i) In an arbitrary figure $\mathcal{F}$ having the actual (crisp) symmetry $\mathbf{G}_A \subset \mathbf{C}_{\infty v}$, there exist points belonging to orbits $\Omega(P, \mathbf{C}_n, Z) \in \mathcal{F}$ with *arbitrary* n ($n = 1, 2, \ldots, \infty$). Around a rotation point Z chosen within $\mathcal{F}$, one has a maximal circle (*vide supra*) which corresponds to the $\mathbf{C}_\infty$ symmetry region, and likewise, we may construct regions $\mathcal{G}(\mathbf{C}_n)$ with multiplicities down to $n = 1$. This means that *every possible rotation symmetry from* $\mathbf{C}_1$ *up to* $\mathbf{C}_\infty$ *(in fact, even up to* $\mathbf{C}_{\infty v}$*) can objectively be found in a given figure* $\mathcal{F}$ (at least as an imperfect[8] symmetry).

(ii) A systematic survey of the orbits within the square $\mathcal{S}q$ (with Z in the barycentre of the figure) is displayed in Figure 5. The idea behind this plot is as follows. Every point of $\mathcal{S}q$ lies on a *maximal orbit* $\Omega_{\max}(P, Z)$ which is the orbit of maximal multiplicity $n_{\max}$ lying entirely in $\mathcal{F}$. In Figure 5, the square is subdivided into regions $\mathcal{G}(n_{\max})$ of points having the same multiplicities of their maximal orbits. The boundaries of these regions are formed by regular $(4 \cdot k)$-gons $\mathcal{P}_{4 \cdot k}$ with $k = 2, 3, \ldots, \infty$, all having the same inradius of unity. These polygons are properly aligned with the square. We have, for instance,

$$\mathcal{G}(4) = \mathcal{P}_4 \setminus \bigcup_{k=2}^{\infty} \mathcal{P}_{4 \cdot k}. \tag{2.10}$$

[8]Symmetries $\mathbf{G}$, for which one finds $\delta(\mathbf{G}) < 1$, have been termed *imperfect* symmetries in [1].

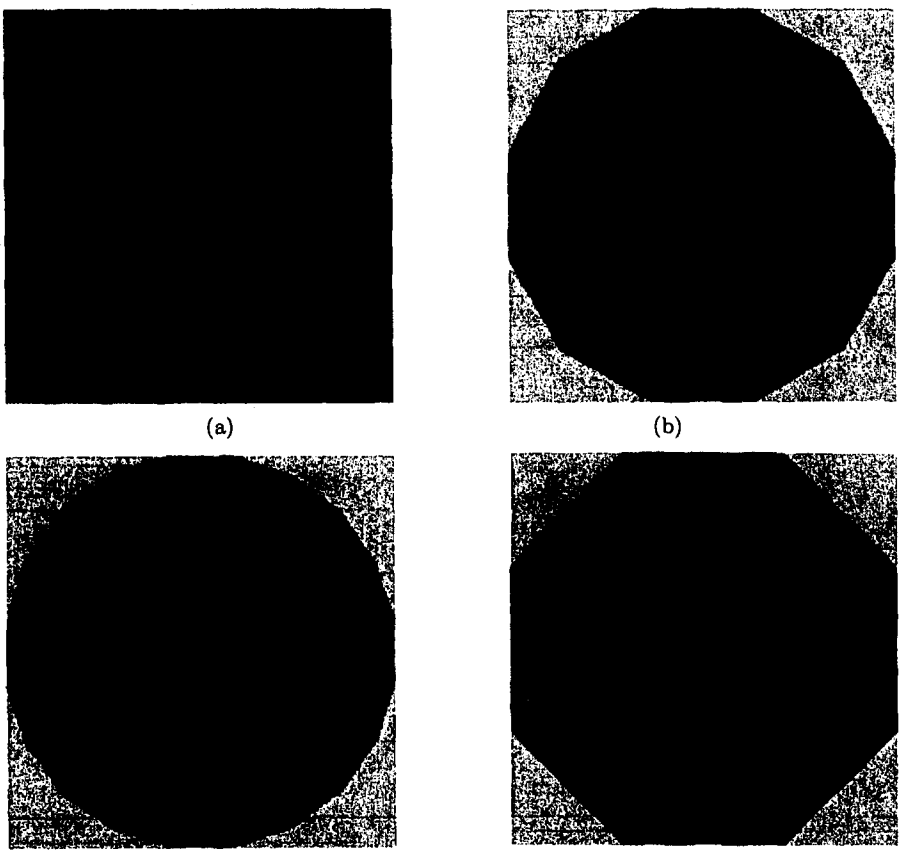

Figure 6. $\mathbf{C}_n$-symmetry (polymetry) regions for a square: dimetry = tetrametry (a), trimetry = hexametry = dodecametry (b), pentametry: an icosagon (c), and octametry (d). The reasons for the identity of different polymetry regions are described in the text.

Then, a $\mathbf{C}_n$-symmetry region can be related to the regions $\mathcal{G}(n_{\max})$. It comprises all regions whose multiplicities $n_{\max}$ are multiples of n (note that some of these may be empty, *vide infra*):

$$\mathcal{G}(\mathbf{C}_n) = \bigcup_{k=1}^{\infty} \mathcal{G}(k \cdot n). \tag{2.11}$$

From the crisp symmetry of the square ($\mathbf{C}_{4v}$), it follows that only multiplicities $n_{\max}$ of $4 \cdot k$ ($k = 1, 2, \ldots, \infty$) can occur. This means, for instance, that any $\mathbf{C}_3$ symmetry in the square must be connected with the $\mathcal{P}_{12}$ polygon (or, generally, $\mathcal{P}_{4 \cdot 3 \cdot k}$) since $\mathcal{G}(3) = \mathcal{G}(6) = \emptyset$. The smallest multiplicity of a $\mathcal{G}(n_{\max})$ region occurring in Figure 5 is four. It corresponds to the multiplicity of the *site symmetry group*[9] $\mathbf{G}_{\text{site}}$ of Z. This is, however, not a necessary feature. As an example, a figure built up by superposing an octagon and a dodecagon (like in Figure 5) also has the crisp symmetry $\mathbf{C}_{4v}$ and the same site symmetry of Z, but in this case, the region $\mathcal{G}(4)$ will be empty.

(iii) Polymetry regions $\mathcal{G}(\mathbf{C}_n)$ for a square with the rotation point Z taken in the barycentre of the figure are displayed in Figure 6. It is clear that, in this case, there cannot exist maximal orbits $\Omega_{\max}(P, Z)$ with multiplicities $n_{\max} \neq 4 \cdot k$ (with $k = 1, 2, \ldots \infty$), since others would destroy the actual symmetry $\mathbf{G}_A = \mathbf{C}_{4v}$ of the square. Therefore, the "strange" symmetries mentioned above can occur *only* as subgroups of supergroups of $\mathbf{G}_A$; strictly

[9]The concept of site symmetry has been used in [6]. In a figure $\mathcal{F}$ having the symmetry $\mathbf{G}_A$, the site symmetry group $\mathbf{G}_{\text{site}}$ of a point Z comprises all symmetry transformations of $\mathbf{G}_A$ that leave Z invariant [4, p. 26; 10]. Thus, $\mathbf{G}_{\text{site}}$ is the crisp symmetry of the figure as seen from Z.

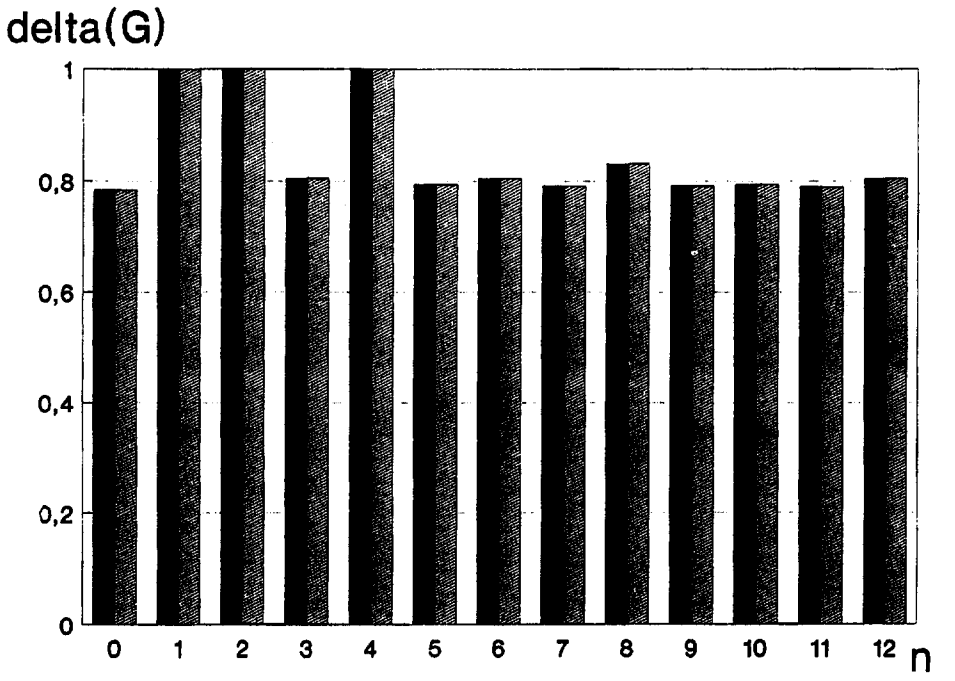

(a)

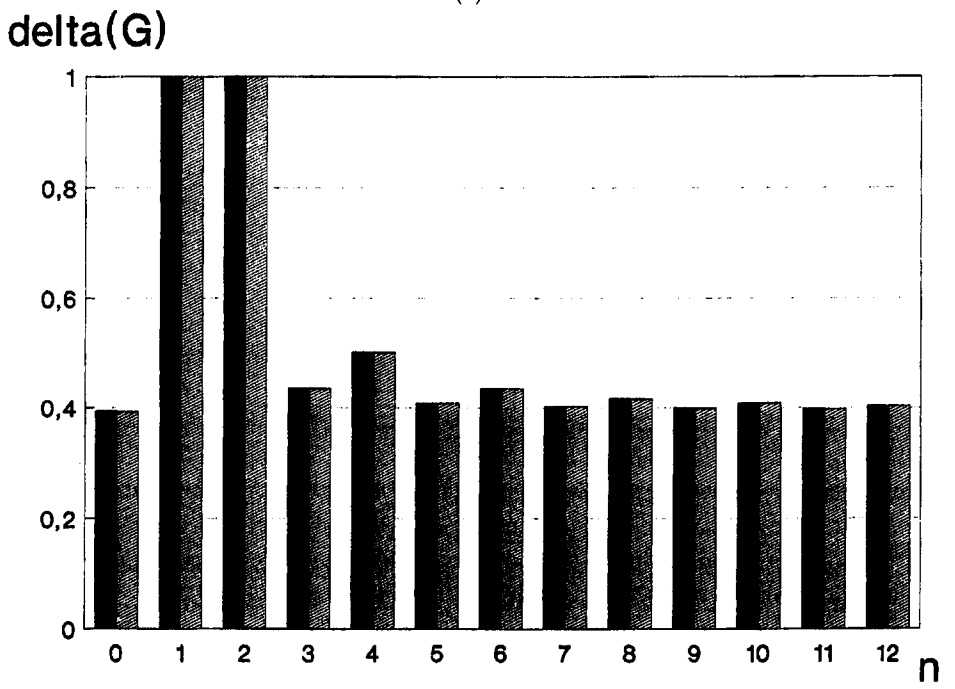

(b)

Figure 7. Symmetry spectra ($\delta(\mathbf{G}) = f(n)$ with $n = 1, \ldots, 12$) for the square $\mathcal{S}q$ and the rectangle $\mathcal{R}e$ based on the areas of polymetry and polysymmetry regions (both regions are identical in every case). The degrees of circularity have been plotted at the position $n = 0$.

speaking, they are $\mathbf{G}_A^{\neq}$ groups as described in Section 2.1. We see that the situation is entirely analogous to that found in the Fourier analysis. The circumstance that a certain symmetry is not present *per se*, but induced by a supergroup can be found out very simply. For the square, e.g., the polymetry regions $\mathcal{G}(\mathbf{C}_3)$, $\mathcal{G}(\mathbf{C}_6)$, and $\mathcal{G}(\mathbf{C}_{12})$ are identical regular

dodecagons (Figure 6b). This indicates that trimetry and hexametry here exist only as subgroup symmetries of dodecametry, as has also been concluded from Figure 5.

(iv) For the square $\mathcal{S}q$ and the rectangle $\mathcal{R}e$, the degrees of symmetry have been calculated from the areas of the different $\mathbf{C}_n$ symmetry regions (with the rotation point Z in the barycentre of the figure). The result is depicted in Figure 7. It can be seen that all kinds of symmetries are present within the square and the rectangle, in particular, also the "strange" symmetries $\mathbf{C}_{3v}$, $\mathbf{C}_{5v}$, $\mathbf{C}_{7v}$, and others. In both cases, no degree of symmetry can be lower than the relative contribution of the maximal circle ($\mathcal{G}(\mathbf{C}_{\infty v})$), since this part of $\mathcal{F}$ contributes to every degree of symmetry.

(v) Size and shape of the polymetry region depend on the position of the rotation point $Z = C_n$, the specific shape of the region being determined by those sides of the figure which the rotation point is next to (see below). For concave geometric figures, a nonvanishing degree of symmetry may also be obtained for positions of the rotation point Z *outside* the figure. An example is sketched in Figure 3c. Here, we find that the symmetry region $\mathcal{G}(\mathbf{C}_2)$ is composed of two nonconnected polygons.

(vi) The symmetry $\mathbf{G}(\mathcal{G}(\mathbf{C}_n))$ of a polymetry region is always a supergroup of the symmetry $\mathbf{C}_n$ tested ($\mathbf{G}(\mathcal{G}(\mathbf{C}_n)) \supseteq \mathbf{C}_n = \mathbf{G}_{\text{test}}$) because additional symmetry elements may interfere (see below).

(vii) The symmetry $\mathbf{G}(\mathcal{G}(\mathbf{C}_n))$ of a polymetry region is always a supergroup of the *site symmetry* $\mathbf{G}_{\text{site}}$ of the rotation point Z, i.e., $\mathbf{G}(\mathcal{G}(\mathbf{C}_n)) \supseteq \mathbf{G}_{\text{site}}$. For example, the symmetry of the tetrametry region with a rotation point Z having the site symmetry $\mathbf{C}_{1v}$ must be (at

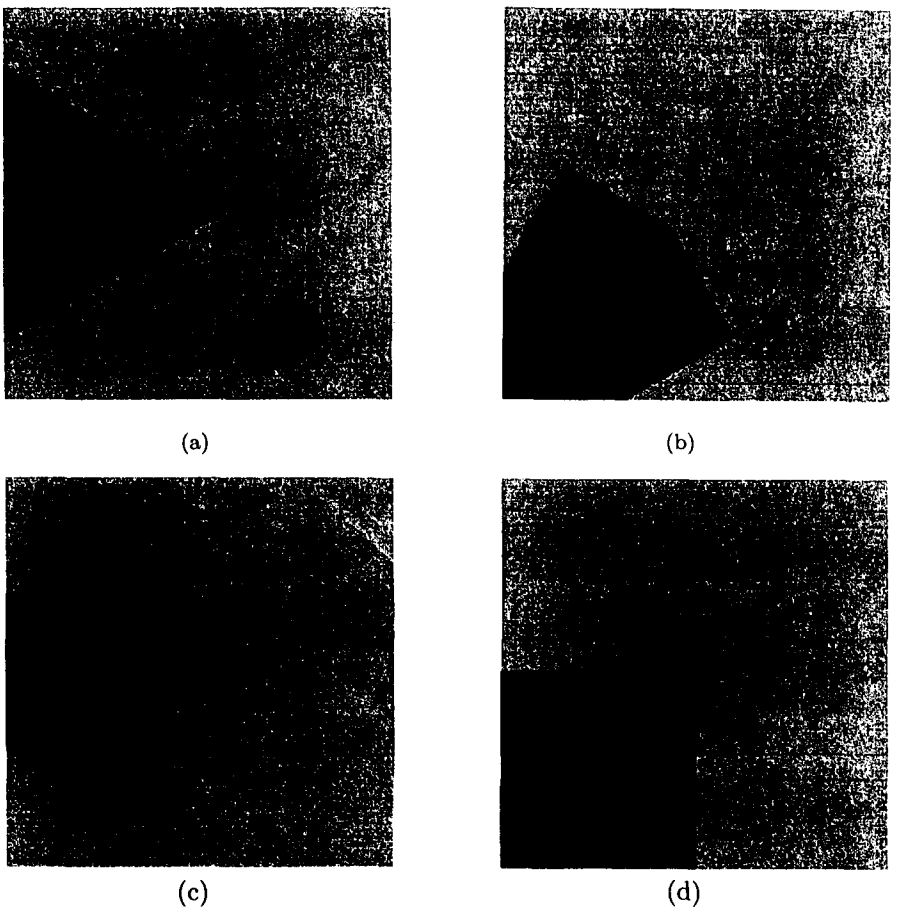

Figure 8. Trimetry (a),(b) and tetrametry (c),(d) regions within a square, when the rotation point Z lies on the horizontal (a),(c) or a diagonal (b),(d) mirror line of the figure, respectively (cf., Figure 9a).

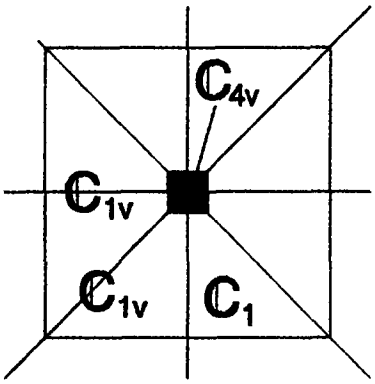

(a) Crisp symmetry elements and site symmetries G_{site} of typical points within a square: C_{4v} in the barycentre, C_{1v} on the mirror lines, and C_1 otherwise.

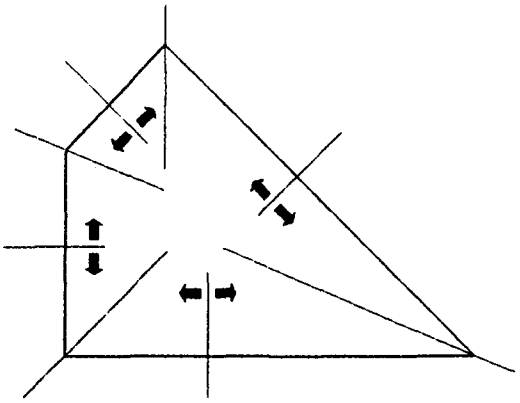

(b) *Local* symmetry elements in figure $Qu1$: in each vertex, a mirror line lies on the angle bisector, and through every point of the sides, we have mirror lines perpendicular to the respective side. All these symmetry elements are *not* symmetry elements of the whole figure.

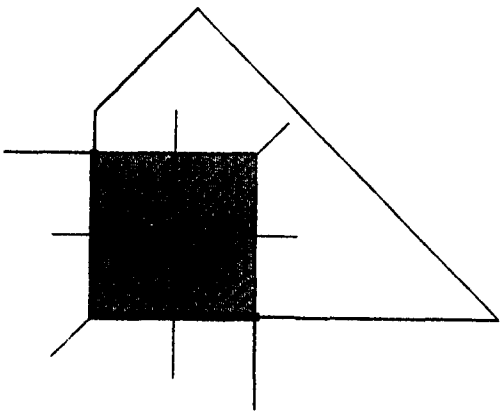

(c) Within $Qu1$, three local mirror lines intersecting Z at appropriate angles induce C_{4v} symmetry of $\mathcal{G}(C_2)$.

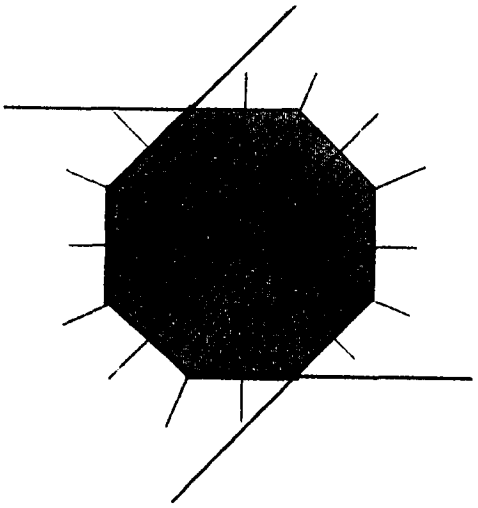

(d) A $\mathcal{G}(C_2)$ region may even have C_{8v} symmetry if Z is intersected by appropriate local mirror lines.

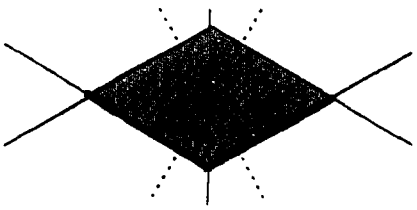

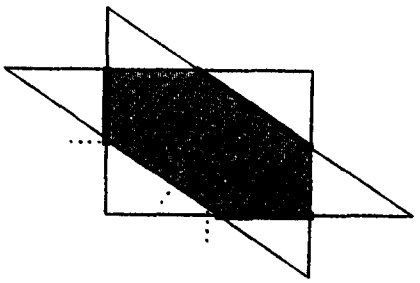

(e),(f) Only one (e) or no (f) mirror line matches the requirements for being a symmetry element of G_{local}, see text. In (c–f), $\mathcal{G}$-segments of $\partial\mathcal{F}$ have been drawn in bold, local mirror lines are drawn as full lines if they are members of G_{local} and as broken lines otherwise.

Figure 9.

least) $\mathbf{C}_{4v}$. This is shown in Figure 8 for the trimetry and tetrametry regions within a square, when the rotation points of these regions lie on the mirror lines of the figure which are depicted in Figure 9a.

(viii) The symmetry of a polymetry region reflects also *local* symmetry elements of the figure which are *not* crisp symmetry elements of the whole figure. As an example, such purely

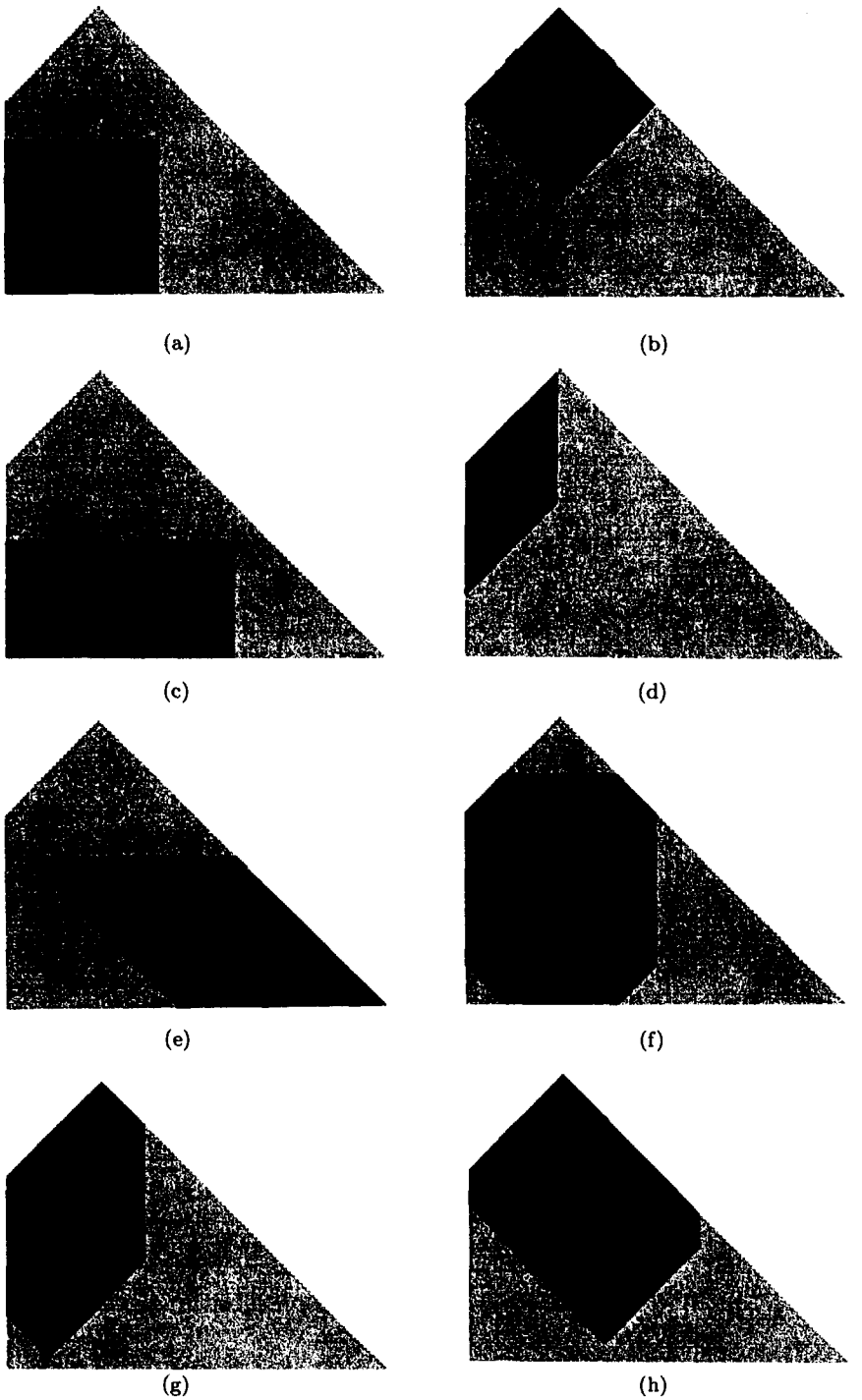

Figure 10. Variation in shape and symmetry of dimetry regions for different positions of the rotation point Z within figure $Qu1$ ($\mathbf{G}_A = \mathbf{C}_1$) and their dependence on local symmetries. The dimetry regions have the following symmetries: $\mathbf{C}_{4v}$ (a),(b), $\mathbf{C}_{2v}$ (c)–(f), and $\mathbf{C}_2$ (g),(h), cf., Figure 12a.

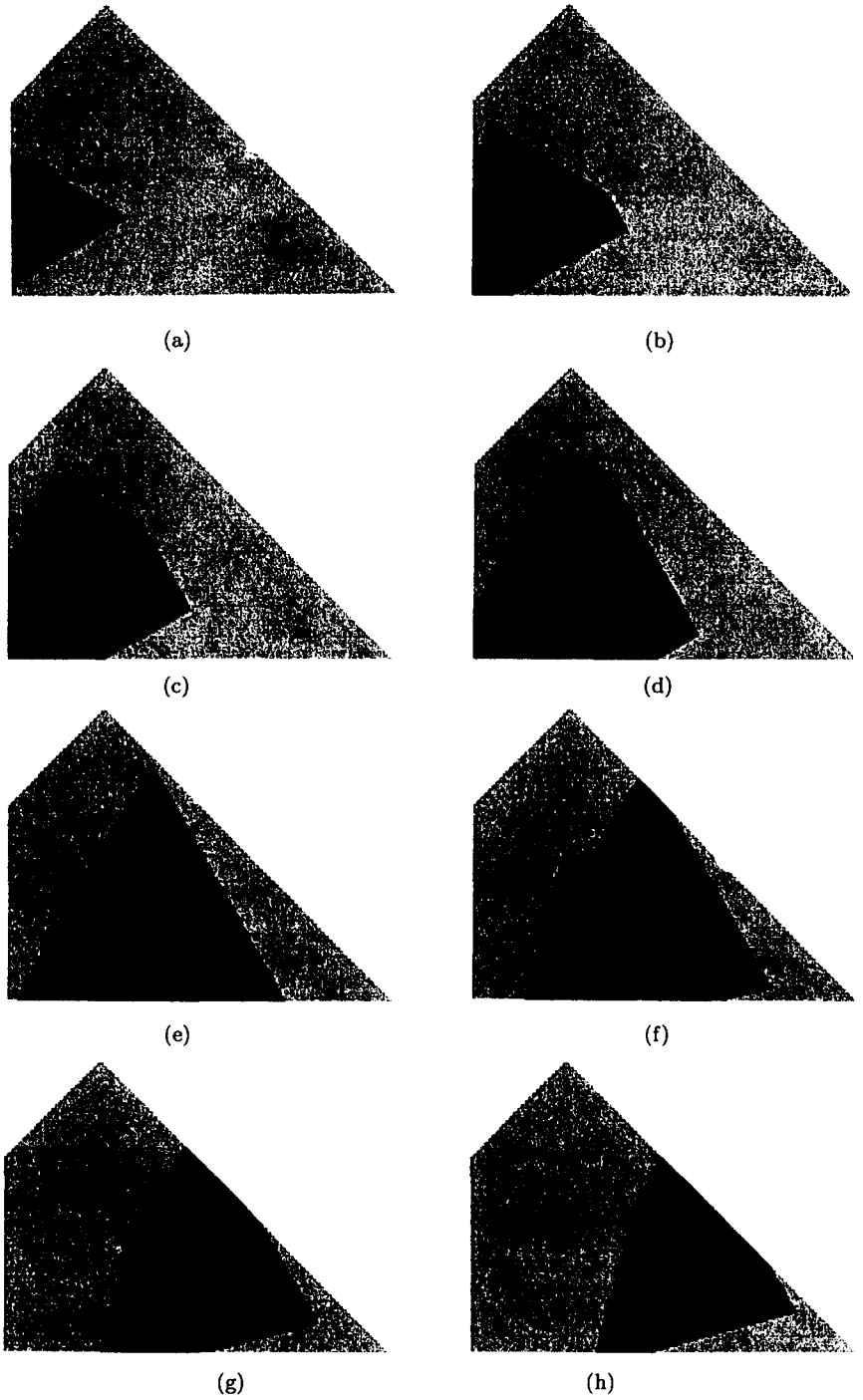

Figure 11. Variation in shape and symmetry of the trimetry region in dependence on the local symmetry: the rotation point Z is shifted within figure $\mathcal{Q}u1$ at $y = 40$ from the left to the right. The corresponding x values are 20 (a), 30 (b), 40 (c), 55 (d), 75 (e), 90 (f), 103 (g), 112 (h), cf., Figure 12b. The symmetries of the trimetry region found here are $\mathbf{C}_{3v}$ (a),(c),(e), and (g) and $\mathbf{C}_3$ (b),(d),(f), and (h).

local symmetry elements of figure $\mathcal{Q}u1$ are sketched in Figure 9b. $\mathcal{Q}u1$ has four local mirror lines on the angle bisectors through its vertices and infinitely many local mirror lines that perpendicularly intersect its sides. Examples of dimetry and trimetry regions in $\mathcal{Q}u1$ whose $\mathbf{C}_{nv}$ symmetry is induced by local mirror lines are shown in Figures 10a–10f and Figures 11a, 11c, 11e, and 11g (compare also Figures 12a and 12b). In Figures 10c

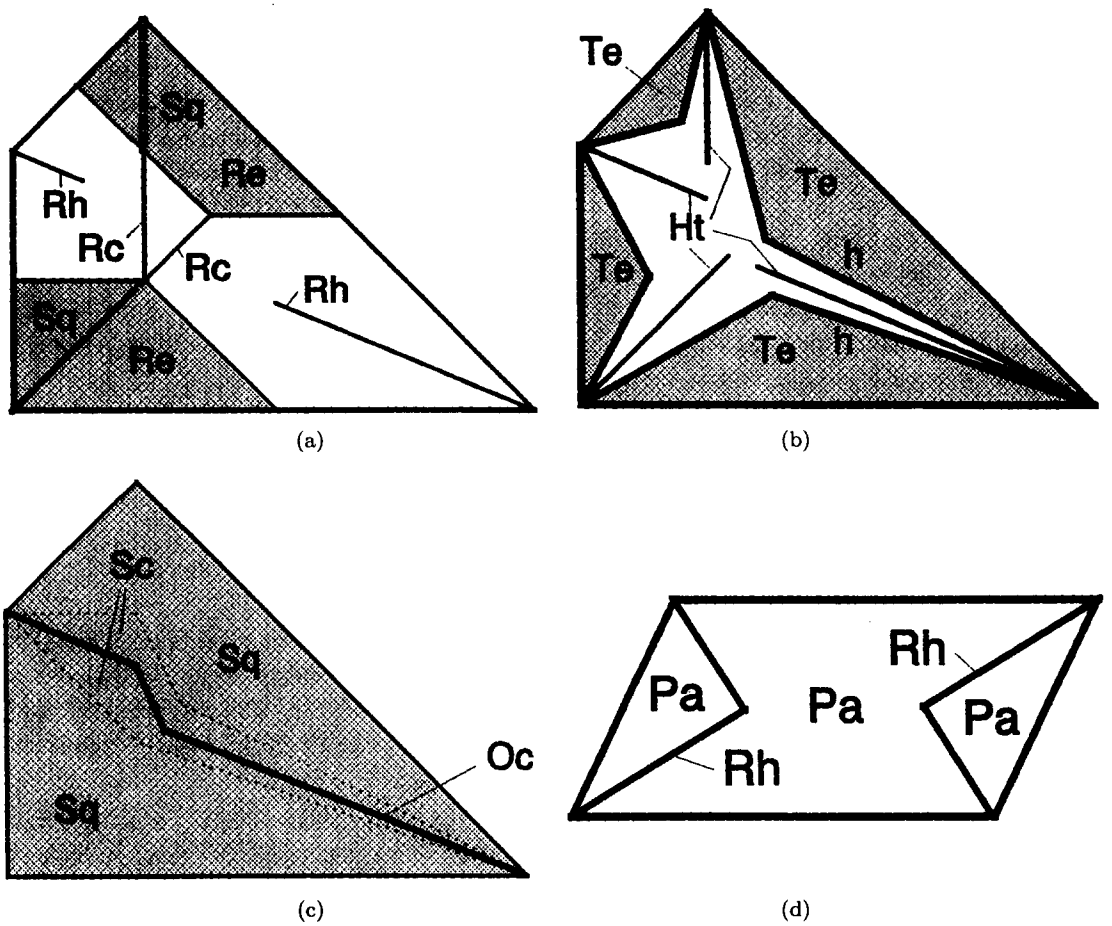

Figure 12. (a)–(c): Diagrams displaying the symmetries of the dimetry (a), trimetry (b), and tetrametry (c) regions within figure *Qu*1 if the position of the rotation point Z varies throughout the figure. In (d), the symmetries of the dimetry regions in a parallelogram are indicated. See text.

and 10f, the rotation point Z lies on *two* local mirror lines, in Figures 10a and 10b even on *three* such lines (cf., Figure 9b) which in the latter case induce a *fourfold* symmetry of $\mathcal{G}(\mathbf{C}_2)$. In sum, if the wandering rotation point $Z = C_n$ comes to coincide with a local mirror line σ, then the polymetry region must get a $\mathbf{C}_{nv}$-symmetric shape, since C_n and σ are generating elements of this group. In Figure 11, Z travels along a line at $y = 40$ and repeatedly meets a local mirror line (Figures 11a, 11c, 11e, and 11g), but in between the symmetry of the trimetry region is only $\mathbf{C}_3$ (Figures 11b, 11d, 11f, and 11h, cf., Figure 12b).

In Figures 9e and 9f, it is shown that local mirror lines will not always become members of the local symmetry group $\mathbf{G}_{\text{local}}$. Therefore, we have to develop the prerequisites for a local mirror line to manifest itself in the symmetry of $\mathcal{G}(\mathbf{C}_n)$. We note that the sides of $\mathcal{G}(\mathbf{G})$ are formed in part by points of $\partial\mathcal{F}$ and in part by points of $\mathcal{F} \setminus \partial\mathcal{F}$.[10] Segments of $\partial\mathcal{F}$ which form sides of $\mathcal{G}(\mathbf{G})$ will be termed $\mathcal{G}$-segments, and vertices of $\mathcal{F}$ which also form vertices of $\mathcal{G}(\mathbf{G})$, analogously, $\mathcal{G}$-vertices. Then it is possible to formulate the influence of local symmetry elements on the symmetry of $\mathcal{G}(\mathbf{G})$ more concisely. Symmetry elements of the *local* symmetry group $\mathbf{G}_{\text{local}}$ are then as follows.

(i) All symmetry lines which are perpendicular to a $\mathcal{G}$-segment of $\partial\mathcal{F}$ and intersect both Z and the midpoint of the $\mathcal{G}$-segment, *and*

[10]The question of whether a certain point $P_s \in \partial\mathcal{F}$ belongs to $\partial\mathcal{G}(\mathbf{C}_n)$ can be judged from equation (2.1).

(ii) all symmetry lines which are angle bisectors at $\mathcal{G}$-vertices of $\partial\mathcal{F}$ and intersect Z.

These principles governing the influence of local symmetry elements are exemplified for *dimetry* regions in Figures 9c–9f. In Figure 9c, Z lies on the angle bisector of the only $\mathcal{G}$-vertex, and three symmetry lines fulfill the conditions for being members of $\mathbf{G}_{\text{local}}$. As is mostly the case, this list of symmetry elements of $\mathbf{G}_{\text{local}}$ is not exhaustive. However, transformation of a single point in general position by these three mirror lines gives a set of eight points which corresponds exactly to the stereogram (stereographic projection) of $\mathbf{C}_{4v}$ which therefore constitutes $\mathbf{G}_{\text{local}}$. In Figure 9d, there are altogether four midpoint lines and three vertex lines which match the requirements for being symmetry elements of $\mathbf{G}_{\text{local}}$, which results to be $\mathbf{C}_{8v}$. In Figure 9e, only one mirror line matches the conditions (giving $\mathbf{G}_{\text{local}} = \mathbf{C}_{1v}$), whereas in Figure 9f, none of the three candidates enters $\mathbf{G}_{\text{local}}$ so that the local symmetry is $\mathbf{C}_1$.

In effect, the symmetry $\mathbf{G}(\mathcal{G}(\mathbf{C}_n))$ of a symmetry region results from the interference of the three partial symmetries mentioned above: $\mathbf{G}_{\text{test}}$ (the symmetry to be tested), $\mathbf{G}_{\text{site}}$, and $\mathbf{G}_{\text{local}}$. We may write

$$\text{Gen}(\mathbf{G}(\mathcal{G}(\mathbf{G}_{\text{test}}))) = \text{Gen}(\mathbf{G}_{\text{test}}) \cup \text{Gen}(\mathbf{G}_{\text{site}}) \cup \text{Gen}(\mathbf{G}_{\text{local}}), \tag{2.12}$$

where $\text{Gen}(\mathbf{G})$ is the generating set of $\mathbf{G}$.

In the following, we will visualize the *symmetry of symmetry regions* more systematically. For this end, we display the areas within a figure $\mathcal{F}$ where a symmetry region $\mathcal{G}(\mathbf{C}_n)$ has a certain symmetry. As an example, Figure 12 shows the symmetries of the dimetry, trimetry, and tetrametry regions within the figures $\mathcal{Q}u1$ and of dimetry regions in $\mathcal{P}a$ for all possible positions of the rotation point Z. From this figure, we see the following.

(i) The *dimetry* regions in $\mathcal{Q}u1$ (Figure 12a) show $\mathbf{C}_{2v}$ symmetry instead of $\mathbf{C}_2$ as soon as the bordering sides ($\mathcal{G}$-segments of $\partial\mathcal{F}$) cut one another at a right angle (the dimetry regions form *rectangles* within the two areas named "$\mathcal{R}e$", compare Figure 10c). If the rotation point Z, additionally, lies on the local angle bisector intersecting a vertex of $\mathcal{Q}u1$, then the symmetry increases to $\mathbf{C}_{4v}$ (lines "$\mathcal{S}q$" within the "$\mathcal{R}e$" areas: the dimetry region becomes a *square*, cf., Figures 10a and 10b). If Z lies on an angle bisector of a vertex not neighbouring upon an "$\mathcal{R}e$" area, then the dimetry region has $\mathbf{C}_{2v}$ symmetry (lines "$\mathcal{R}h$": the dimetry region becomes a *rhombus*, cf., Figures 10d and 10e). The end points of these lines correspond to maximal rhombi which can be drawn within $\mathcal{Q}u1$. Beyond the end points of these lines, the dimetry region is determined by additional, *skew* bordering sides of $\mathcal{Q}u1$ so that the $\mathbf{C}_{2v}$ symmetry is destroyed. On the "$\mathcal{R}c$" lines, the dimetry region forms a *cut rectangle* with $\mathbf{C}_{2v}$ symmetry (Figure 10f). If Z lies in the remaining areas of figure $\mathcal{Q}u1$, then the dimetry region has only $\mathbf{C}_2$ symmetry (Figures 10g and 10h). To be strict, the vertices of $\mathcal{F}$ form separate *single* points where $\mathcal{G}(\mathbf{C}_2)$ is a *point* and therefore has $\mathbf{C}_{\infty v}$ symmetry, whereas on all sides of $\mathcal{F}$, the dimetry region is always a *line* and has $\mathbf{C}_{2v}$ symmetry.

(ii) The *trimetry* regions of $\mathcal{Q}u1$ display either $\mathbf{C}_3$ or $\mathbf{C}_{3v}$ symmetry (Figure 12b). The latter is found on all angle bisectors by virtue of the influence of these local mirror lines ("$\mathcal{H}t$" lines, the trimetry region is a *trigonal hexagon*, cf., Figures 11c and 11g) and on areas along the sides of $\mathcal{Q}u1$ ("$\mathcal{T}e$" areas, the trimetry region is an *equilateral triangle*, cf., Figures 11a and 11e). The borderlines of these areas are determined by the available height (marked "h" in Figure 12b) or basis width (not marked) for an equilaterally triangular trimetry region. In all cases, the $\mathbf{C}_{3v}$ symmetry is induced by local mirror lines. The $\mathbf{C}_{3v}$ lines along the angle bisectors ("$\mathcal{H}t$" lines) end as soon as the trimetry region reaches the opposite (skew) side of $\mathcal{Q}u1$. On the sides and in vertices of $\mathcal{Q}u1$, the trimetry region is a *point* ($\mathbf{C}_{\infty v}$ symmetry).

(iii) The *tetrametry* regions within $\mathcal{Q}u1$ display $\mathbf{C}_{4v}$ symmetry almost everywhere, except on a line ("$\mathcal{O}c$") running through the whole figure, where we find $\mathbf{C}_{8v}$ symmetry. $\mathbf{C}_4$ symmetry

is completely lacking. This is due to the special shape of figure $\mathcal{Q}u1$, all its sides being compatible with $\mathbf{C}_{4v}$ or even $\mathbf{C}_{8v}$ symmetry of the tetrametry region (i.e., Z is then intersected by multiple mirror lines which induce a local symmetry of $\mathbf{G}_{\text{local}} = \mathbf{C}_{4v}$ or even $\mathbf{C}_{8v}$). Within the "$\mathcal{S}q$" areas, the tetrametry region forms a *square*, but near the $\mathbf{C}_{8v}$ line (within the "$\mathcal{S}c$" region bordered by thin dotted lines), it takes the shape of a *cut square*, likewise of $\mathbf{C}_{4v}$ symmetry. On all sides of $\mathcal{Q}u1$, the trimetry region is a *point* ($\mathbf{C}_{\infty v}$ symmetry).

For the parallelogram $\mathcal{P}a$, the dimetry region is also a parallelogram, displaying $\mathbf{C}_2$ symmetry ("$\mathcal{P}a$" areas), except on the "$\mathcal{R}h$" lines along the angle bisectors, where it is a rhombus with $\mathbf{C}_{2v}$ symmetry, and on the sides of the parallelogram (also $\mathbf{C}_{2v}$ symmetry).

2.4. $\mathbf{C}_{nv}$-Symmetry (Polysymmetry) Regions of a Figure

As could be seen from Figures 6, 8, 10, and 11, in many instances the *polymetry* region of a figure has $\mathbf{C}_{nv}$ symmetry instead of $\mathbf{C}_n$. This means that the polymetry and polysymmetry regions are identical, and the degrees of $\mathbf{C}_n$ and $\mathbf{C}_{nv}$ symmetry are equal for that position of the rotation point Z. If, however, the polymetry region has only $\mathbf{C}_n$ symmetry, the polysymmetry region must be determined separately.

For the determination of polysymmetry regions $\mathcal{G}(\mathbf{C}_{nv})$, both algorithms for the construction of polymetry regions can be extended. The respective object (in the orbit method: the point under consideration; in the figure transformation method: the whole figure $\mathcal{F}$) is transformed by all operations of $\mathbf{C}_{nv}$. The problem is, however, that the angular orientation ε of the set of n mirror lines is not clear *a priori*. In fact, for arbitrary values of ε a symmetry region $\mathcal{G}(\mathbf{C}_{nv}, Z, \varepsilon)$ can be constructed. Therefore, we vary ε between 0 and π/n, and evaluate the *optimum orientation* ε_{opt}, i.e., the one giving a maximum value of $\delta(\mathbf{C}_{nv}, \varepsilon)$. This means that in the following, we are always speaking of *maximal* polysymmetry regions. In the case of a $\mathbf{C}_n$ region having already $\mathbf{C}_{nv}$ symmetry, the maximal $\mathbf{C}_{nv}$ region is identical with that $\mathbf{C}_n$ region.

In many simple cases, dimetry regions are parallelograms. What, then, is the corresponding disymmetry region? And how does its orientation ε depend on the side lengths ratio of the parallelogram? This can be seen from Figure 13. Here, the longer sides (200 pixels long) of the parallelograms are always parallel to the x axis, the angles within the figures are 45° and 135°, and the lengths of the shorter sides are varied from 0 up to 200 pixels (a rhombus). The resulting degrees of symmetry are displayed in Figure 13. It shows that the optimum mirror line orientation ε_{opt} varies from 0° (i.e., parallel to the longer sides; this is the limit orientation for an infinitely long parallelogram) to 22.5° (the diagonal direction for a 45° rhombus). The nonlinearity of this dependence can be easily seen from the bold line connecting the ε_{opt} values for the different parallelograms (Figure 13b).

To illustrate the nontrivial problem of the optimum mirror line orientation more specifically, *angular symmetry profiles* for $\mathbf{C}_{2v}$ have been determined for the right triangle $\mathcal{T}r1$ by varying the orientation angle ε of the set of mirror lines for a fixed position of Z. Figures 14a–14c display these profiles for different positions of the rotation point Z in $\mathcal{T}r1$ (varied along a line with $y = 40$). We see that the angular profiles can be very complex, in particular, we may may find multiple side-maxima which in the variation of the Z position may become predominant. In Figures 14a and 14b, the succession of profiles from bottom to top shows such a side maximum growing up to predominance (in Figure 14b). This process results in an abrupt jump in the position of the optimal mirror line orientation (Figure 14d) for $x_Z = 39 \rightarrow 40 \rightarrow 41$. (Note that at $Z = (40, 40)$, the rotation point lies on the angle bisector of point A whose orientation angle is 45°.) Thus, the optimal mirror line orientation ε_{opt} may change within a very narrow Z position interval, so that a precise determination of it can require a very small steplength in the angle variation. On the other hand, the optimal mirror line orientation may also shift *continuously* over a broader x_Z interval (Figure 14d, $x_Z > 47$). Here, also the supposed jump in ε_{opt} at $x_Z = 47$ is in reality

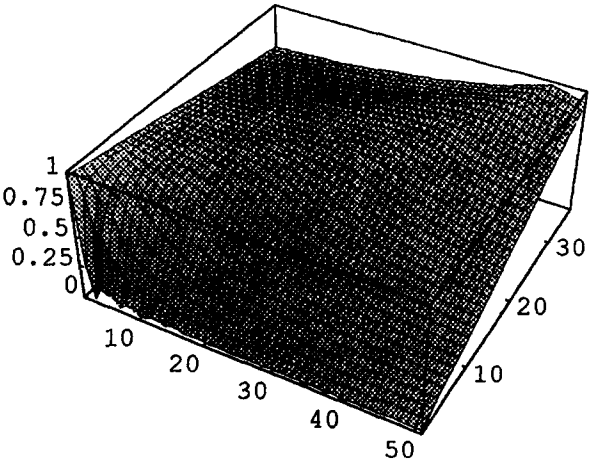

(a)

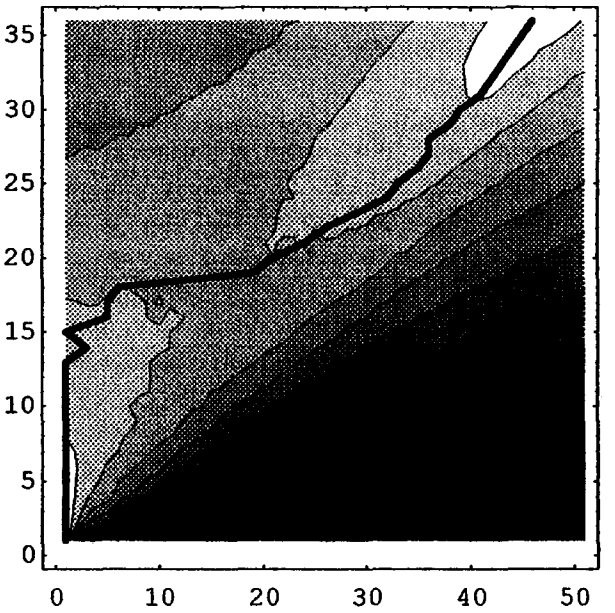

(b)

Figure 13. Optimal orientation ε_{opt} of the set of two mirror lines of the disymmetry region in parallelograms with fixed length (200 pixels) of their longer sides and varying length of the shorter sides: along the x coordinate, the mirror line orientation angle ε has been varied in 50 steps à 0.5° from 0° to 25°; along the y axis, the altitude of the parallelogram has been varied in 36 steps à 4 pixels from 0 to 140 pixels (corresponding to a shorter side length of 198 pixels, approximately a rhombus). In (b), the optimal orientation angles ε_{opt} (giving a maximal degree of symmetry) are connected by a bold line.

a *continuous* shift from 0° to *negative* angles; the second $\mathbf{C}_{2v}$ mirror line shifts from 90° down to ca. 59°. In general, if Z is located near a side of $\mathcal{F}$, then ε_{opt} for $\mathcal{G}(\mathbf{C}_{2v})$ is parallel to that side. In Figure 14d, the corresponding orientations are $\varepsilon_{\text{opt}} = 0°$ for $x_Z \to 0$ and $\varepsilon_{\text{opt}} = -30.96°$ (or $\varepsilon_{\text{opt}} = 59.04°$) for $x_Z \to 133.\bar{3}$, the point where the $(y = 40)$-line crosses the triangles's borderline. Towards the centre of $\mathcal{F}$, new maxima arise in the angular symmetry profile (Figure 14c) which vary in height and may give rise to the abrupt changes in the optimal mirror line orientation.

The determination of polysymmetry regions is often more laborious than that of polymetry regions, but nevertheless, it is always possible for positions $Z \in \mathcal{F}$, so that we can generalise the result of the foregoing chapter. *Every possible symmetry from* $\mathbf{C}_1$ *up to* $\mathbf{C}_{\infty v}$ *can objectively be found in a given figure* $\mathcal{F}$ (at least as an imperfect symmetry).

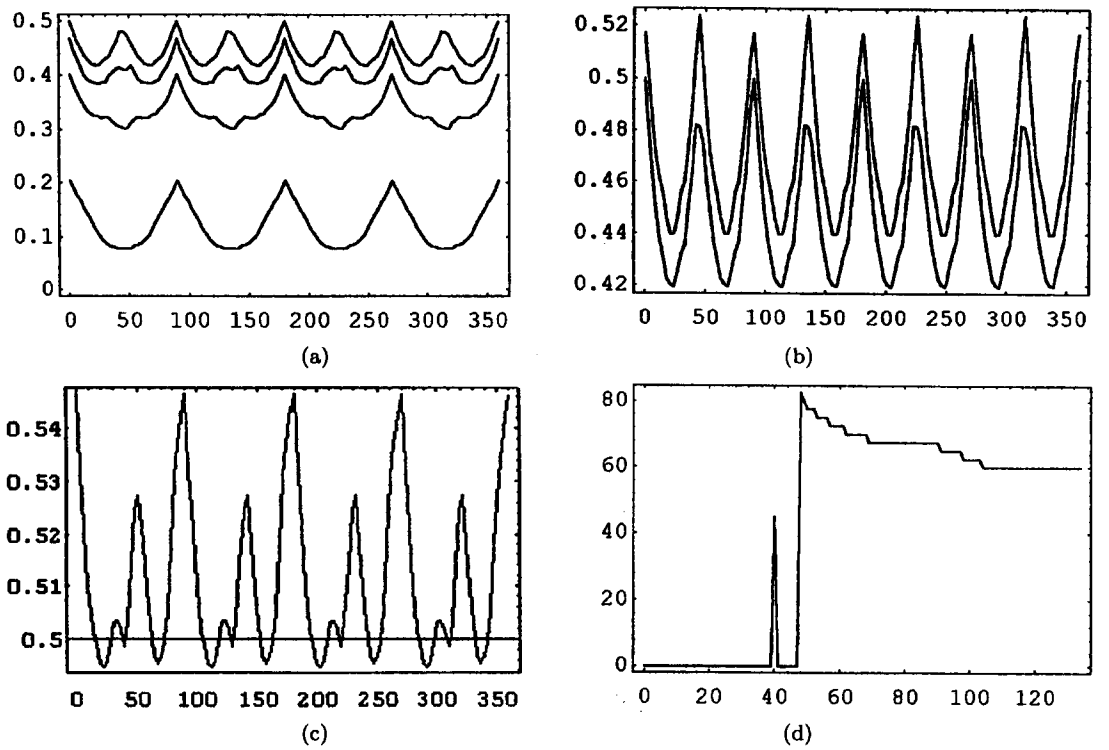

Figure 14. Angular symmetry profiles $\delta(\mathbf{C}_{2v}) = f(\varepsilon)$ for disymmetry regions in the figure $\mathcal{T}r1$ when varying the rotation point position x_Z along a line with $y = 40$; (a): from bottom to top: $x_Z = 15, 30, 35, 38$; (b): from bottom to top: $x_Z = 38, 40$; (c): $x_Z = 45$; (d): the optimal mirror orientation ε_{opt} (in degrees) for the variation of x_Z from 0 to $133.\bar{3}$.

2.5. Symmetry Profiles and Landscapes for a Geometric Figure

As follows from the definition of an orbit, the size of a polymetry region within a geometric figure $\mathcal{F}$ (and therefore, also the degree of symmetry derived from its area) depends on the position of the rotation point Z. A variation of this position then gives a *symmetry profile* or a *symmetry landscape* of the figure if $\delta(\mathbf{G}, Z)$ is plotted as a function of the coordinates of Z. Examples of symmetry profiles are given in Figures 15 and 16.

The polymetry profiles (Figure 15) display the following features.

(i) If the rotation point Z moves at right angles off a straight side of the figure, then the polymetry regions for $\mathbf{C}_n$ ($n \geq 3$) have $\mathbf{C}_{nv}$ symmetry due to a local mirror line; they are regular n-gons (or a circle). Therefore, their area increases *parabolically* with the distance of Z from the side (proportional to the square of the inradius), and the symmetry profile is parabolic (Figures 15a and 15d—left side). If the side of the figure is not straight but angular (acute), the profile is parabolic with a lower proportionality factor (Figures 15b and 15d—right side). However, near angular sides with *re-entrant* angles, also trimetry and other regions may deviate drastically from a parabolic profile (Figures 15e and 15f—left sides) if the polymetry region has a pronounced n-fold star shape (cf., Figure 3d).

(ii) In the case of a straight side, the symmetry profile for dimetry fails to be parabolic (see Figures 15a and 15d—left side). This is due to the special role played by C_2 in this case. The C_2 rotation transforms a straight line into a parallel straight line without giving a closed polygon, so that dimetry is compatible with an *infinite* elongation of a figure, and the shape and size of the dimetry region are determined by more than one side of $\mathcal{F}$. Therefore, the dimetry profile may strongly deviate from being parabolic. In contrast, near acute sides the shape of the dimetry region is determined by these two sides only, and the dimetry profile becomes parabolic (Figures 15b and 15d–15f—right sides).

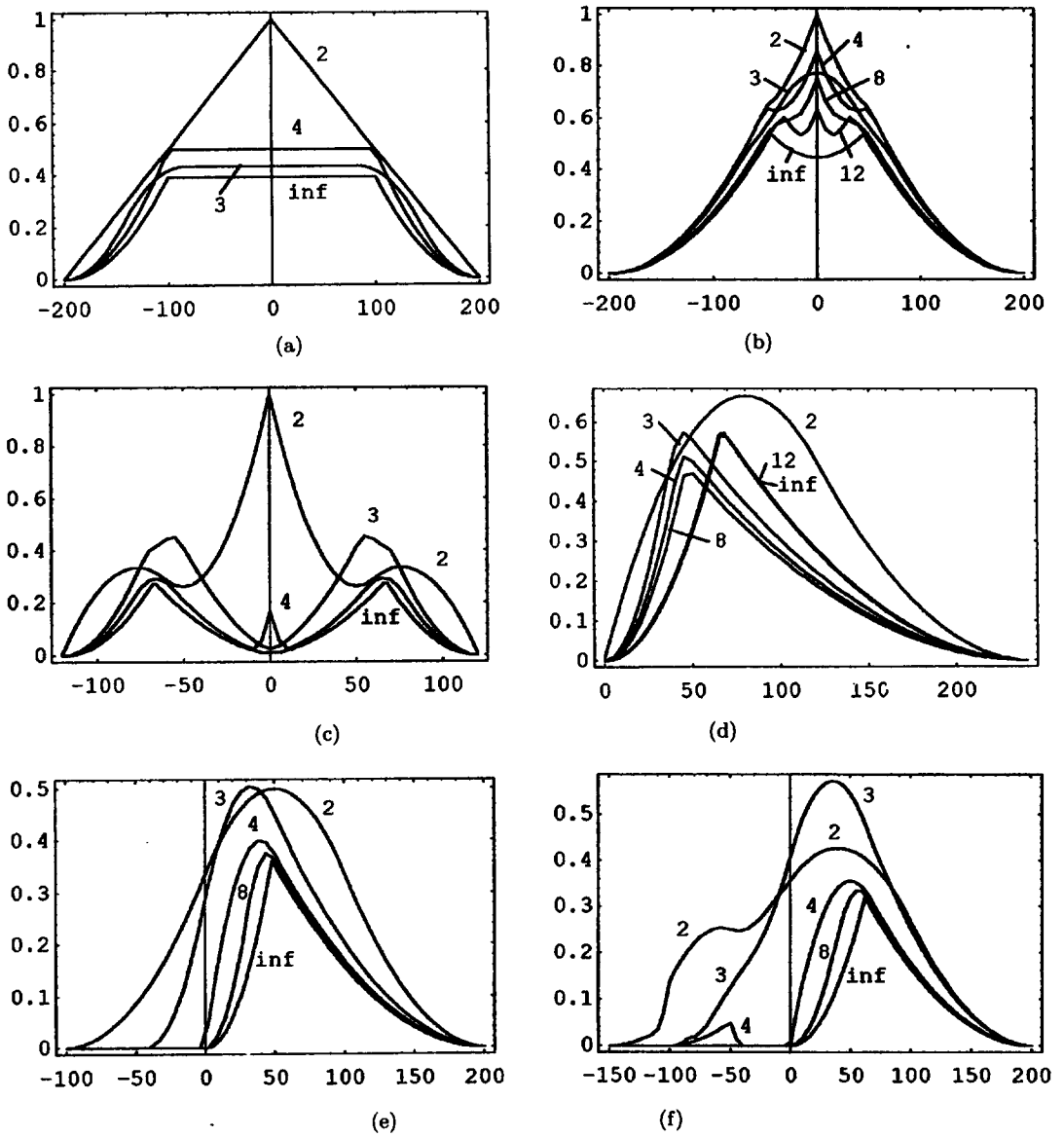

Figure 15. Polymetry profiles along the symmetry line (taken as x axis) for the figures $\mathcal{R}e$ (a), $\mathcal{O}e$ (b), $\mathcal{S}w$ (c), $\mathcal{T}ia$ (d), $\mathcal{A}r$ (e), and $\mathcal{O}p$ (f). The figures $\mathcal{R}e$, $\mathcal{O}e$, and $\mathcal{S}w$ are positioned with their symmetry centres in the origin. The multiplicity n of the polymetry tested is indicated in the plots ("inf" = ∞).

(iii) Near a straight side, $\mathcal{G}(\mathbf{C}_n)$ will for $n \geq 3$ take the shape of a closed regular n-gon which is in a coarse sense "circular" and for increasing n approaches a circle. Therefore, the maxima of trimetry, etc., are often located near the maximum of circularity. In any case, the maxima of polymetry converge to the circularity maximum for increasing n.

(iv) Symmetry profiles may extend beyond the boundaries of the figure if it displays re-entrant angles (Figures 15e and 15f). In this case, one finds a certain area of overlap between the original ($\mathcal{F}$) and transformed ($\mathcal{F}^{(k)}$) figures also for positions of Z *outside* the figure (cf., Figure 3c).

(v) The symmetry profile may even decompose into more than one nonvanishing part. In Figure 15f ($n = 4$), the left maximum marks the centre of the roughly fourfold symmetric "hole" in the figure $\mathcal{O}p$.

Polymetry and polysymmetry profiles are compared in Figure 16. As already stated, the degrees of polymetry and polysymmetry are equal if the polymetry region has $\mathbf{C}_{nv}$ symmetry

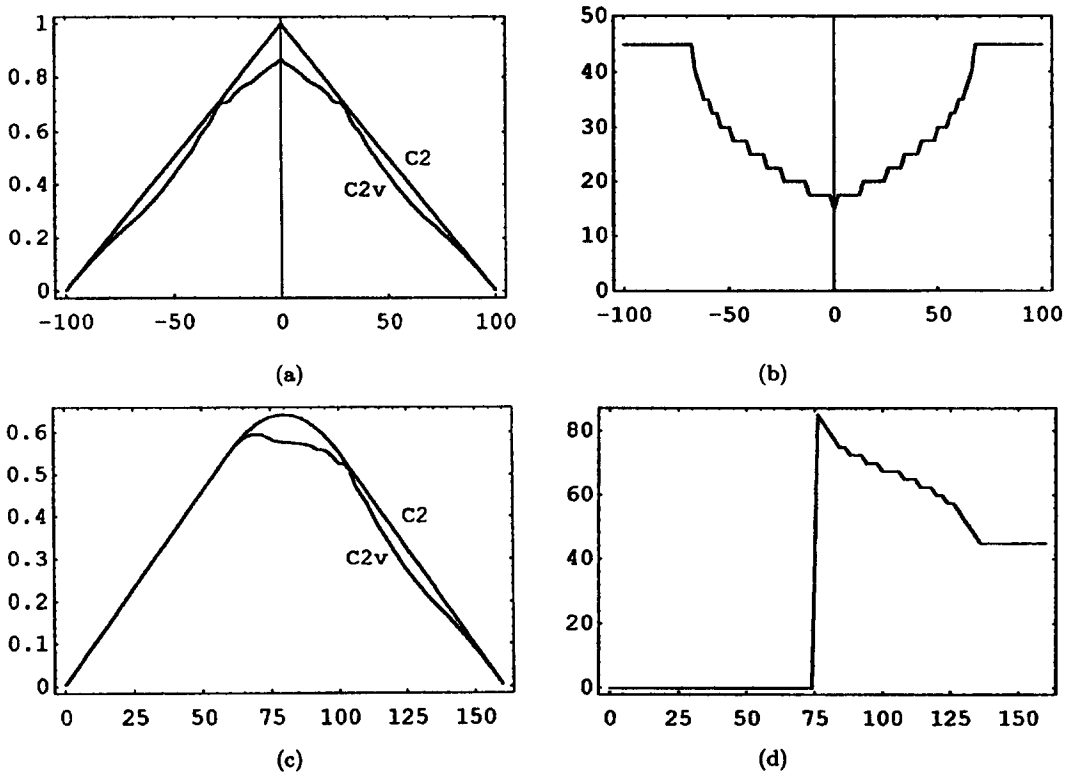

Figure 16. Linear symmetry profiles (a),(c) for dimetry ("C2") and disymmetry ("C2v") through figure $\mathcal{P}a$ along the symmetry line with the symmetry centre in the origin (a),(b) and through $\mathcal{Q}u1$ along a line at $y = 40$ (c),(d), together with the corresponding optimal mirror line orientation profiles $\varepsilon_{\text{opt}} = f(x)$ (b),(d). The orientation angles are given in degrees. See text.

instead of $\mathbf{C}_n$. In Figure 16a, both profiles are shown for the parallelogram $\mathcal{P}a$. Here, we have $\delta(\mathbf{C}_{nv}) = \delta(\mathbf{C}_n)$ at four points. First, these are the starting and end points ($x_Z = \pm 100$) where the regions $\mathcal{G}(\mathbf{C}_{2v})$ and $\mathcal{G}(\mathbf{C}_2)$ comprise only the pixels of the shorter side lines of the parallelogram and, therefore, necessarily have $\mathbf{C}_{2v}$ symmetry. Second, this equality is found at $x_Z \approx \pm 30$. Here, the angle bisectors of the vertices adjacent to the shorter sides of $\mathcal{P}a$ ("$\mathcal{R}h$" lines in Figure 12d) intersect. On these "$\mathcal{R}h$" lines, the dimetry regions are rhombi and display $\mathbf{C}_{2v}$ symmetry. The corresponding optimal mirror line orientations ε_{opt} are displayed in Figure 16b. Comparing with Figure 12d, we see that at $x_Z = \pm 100$, the mirror lines are parallel to the shorter sides of $\mathcal{P}a$ (45°). With increasing altitude of the $\mathcal{G}(\mathbf{C}_2)$-parallelogram, ε_{opt} shifts to values below 20°. The points $x_Z \approx \pm 30$ with $\delta(\mathbf{C}_2) = \delta(\mathbf{C}_{2v})$ and $\varepsilon_{\text{opt}} = 22.5°$ are, however, not prominent in the ε_{opt} plot.

In Figure 16c, the dimetry and disymmetry profiles are shown for a line at $y = 40$ through figure $\mathcal{Q}u1$. Figure 16d shows the corresponding optimal mirror line orientations. These profiles for $\mathcal{Q}u1$ can immediately be compared with Figure 12a: as long as we are moving through the "$\mathcal{R}e$" area, we have $\delta(\mathbf{C}_{2v}) = \delta(\mathbf{C}_2)$ and $\varepsilon_{\text{opt}} = 0°$ (or $\varepsilon_{\text{opt}} = 90°$). After leaving the "$\mathcal{R}e$" area, the degrees of polymetry and polysymmetry become different up to $x_Z \approx 102$, where we reach the end of the "$\mathcal{R}h$" line (the dimetry region is a *rhombus*), where the optimal mirror lines are at $-22.5°$ or $+67.5°$. After a second x_Z interval with different degrees of symmetry, we reach the right side of $\mathcal{Q}u1$ at $x_Z = 160$, where both degrees of symmetry anew become equal and the mirror line is along the polygon side ($\varepsilon_{\text{opt}} = \pm 45°$). In Figure 16d, the jump in ε_{opt} at $x_Z = 75$ is in reality a *continuous* shift from 0° to *negative* angles; the second $\mathbf{C}_{2v}$ mirror line shifts from 90° down to 45°.

Examples of polymetry *landscapes* are shown in Figure 17. The symmetry landscapes also display important features we already saw in the symmetry profiles.

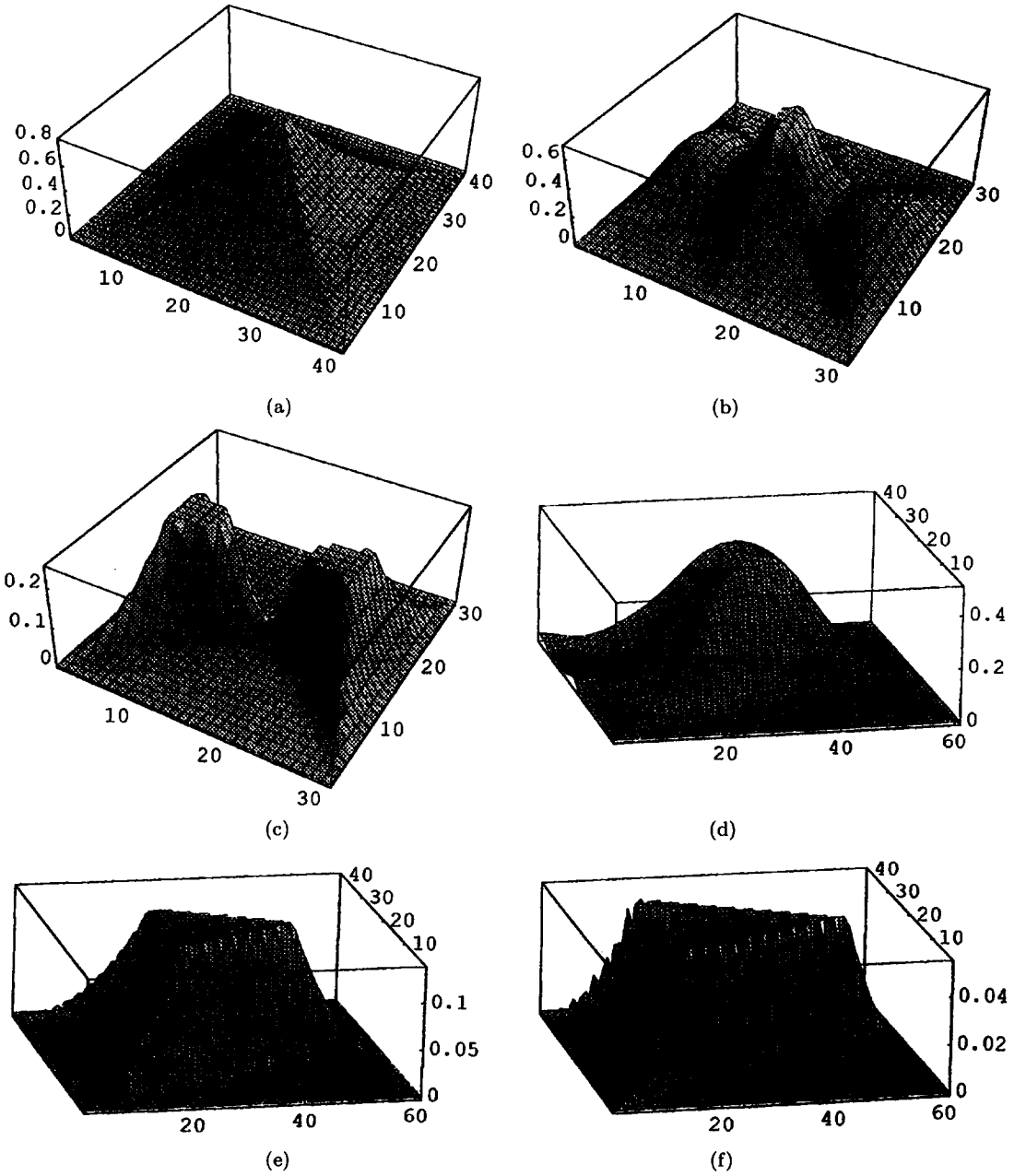

Figure 17. Symmetry landscapes for circularity in the square $\mathcal{S}q$ (a), for dimetry (b), and trimetry (c) in the swallow-tail figure $\mathcal{S}w$, and for dimetry (d), trimetry (e), and octametry (f) in the arrowhead figure $\mathcal{A}r$. Numbers at the x, y axes are step numbers, not coordinates.

(i) Near straight sides, the degree of symmetry (except for $\mathbf{C}_2$) varies parabolically. This can be best seen in the circularity profile for the square $\mathcal{S}q$ in Figure 17a. The corresponding dimetry profile for $\mathcal{S}q$ is a simple square pyramid.

(ii) The symmetry landscapes—like the symmetry profiles—may extend beyond the boundaries of the geometric if it has re-entrant angles. However, in the landscapes the varying extent of this phenomenon is even more pronounced. The convergence of the landscapes for increasing n towards the one for $\mathbf{C}_{\infty v}$ can easily be seen (Figures 17b, 17c, and 17d–17f). For $\mathbf{C}_{\infty v}$ landscapes, the degree of symmetry can be nonvanishing only if the rotation point Z lies *within* the figure. In accordance with this, for the $\mathcal{A}r$ figure, the "tail" of the symmetry landscape along the negative x axis decreases in length for increasing n (Figures 17d–17f).

(iii) Surprisingly, for the *Ar* and *Sw* figures, we get pronounced *plateaus* in the $\delta(\mathbf{C}_n)$ landscapes (especially for higher values of n), indicating that there are only minor variations in the area of the polymetry regions in the inferior of the figures.

In sum, the symmetry landscapes (like the symmetry profiles) provide a detailed characterisation of a given geometric figure $\mathcal{F}$ with respect to the different symmetries (and separately for polymetry and polysymmetry properties). That the local symmetry properties of a figure may be very different for different multiplicities n of the rotation point is documented in Figures 17b and 17c for $\mathbf{C}_2$ and $\mathbf{C}_3$.

2.6. Symmetry Centroids of a Geometric Figure

The symmetry landscape for a figure $\mathcal{F}$ corresponds to a two-dimensional spatial distribution of the degree of symmetry over the area of the figure.[11] Therefore, the position $Z_\mathbf{G} = (x_\mathbf{G}, y_\mathbf{G})$ of a **G**-*symmetry centroid* can be calculated using the symmetry landscape $\delta(\mathbf{G}, Z)$ as a weighting function in the process of averaging:

$$x_\mathbf{G} = \frac{\int_A \mathrm{d}A{\cdot}x_Z \cdot \delta(\mathbf{G}, Z)}{\int_A \mathrm{d}A{\cdot}\delta(\mathbf{G}, Z)}, \qquad y_\mathbf{G} = \frac{\int_A \mathrm{d}A{\cdot}x_Z \cdot \delta(\mathbf{G}, Z)}{\int_A \mathrm{d}A{\cdot}\delta(\mathbf{G}, Z)}, \tag{2.13}$$

or, for discretely varying Z positions,

$$x_\mathbf{G} = \frac{\sum_Z x_Z \cdot \delta(\mathbf{G}, Z)}{\sum_Z \delta(\mathbf{G}, Z)}, \qquad y_\mathbf{G} = \frac{\sum_Z x_Z \cdot \delta(\mathbf{G}, Z)}{\sum_Z \delta(\mathbf{G}, Z)}, \tag{2.14}$$

where the summation is over all discrete positions of Z.

Table 2. x-positions of the polymetry centroids for different figures having a symmetry line (taken as x axis so that all y positions of the centroids are zero). The barycentres are used as reference points (0,0). Their absolute positions have been calculated from the barycentre formula for triangles (B_calc) and also taken from the discrete figures (B_pix) to illustrate the accuracy of the discrete calculation. The position of the circularity centroid has been calculated with the *Mathematica* program [9] and shifted by subtracting B_calc.

n	*Tia*	*Tio*	*Ar*	*De*
1	0	0	0	0
2	−0.001	−0.003	0.000	+0.001
3	−5.606	2.519	1.133	−4.823
4	−5.481	2.862	8.320	−7.140
5	−5.127	2.754	9.352	−6.821
6	−5.374	2.737	9.729	−6.779
8	−5.322	2.754	10.309	−6.872
12	−5.365	2.747	10.659	−6.887
∞	−5.315	2.747	11.087	−6.841
B_calc	80	40	$33.\bar{3}$	$133.\bar{3}$
B_pix	80.061	39.872	33.165	133.499

When comparing the symmetry centroids of a figure $\mathcal{F}$ for different symmetries **G**, one finds that in figures having only $\mathbf{C}_{1v}$ or $\mathbf{C}_1$ symmetry, the symmetry centroids no longer coincide with the barycentre of the figure. The latter is evaluated by using $\delta(\mathbf{C}_1, Z) = 1$, i.e., the barycentre can be regarded as the monometry centroid.[12] Data for the polymetry centroids of figures having

[11] In principle, we have $Z \in \mathbb{R}^2$. This is relevant, however, only for monometry. For *convex* polygons, it is sufficient to vary the position of Z only *within* the figure. For *concave* polygons $\mathcal{F}$, Z needs to be varied only within a corresponding convex polygon $\mathcal{F}^+$ which is $\mathcal{F}$ augmented by all points lying on lines connecting two points of $\mathcal{F}$: $\mathcal{F}^+ = \mathcal{F} \cup \{P \notin \mathcal{F} \mid P \in \overline{P_1P_2} \wedge P_1, P_2 \in \mathcal{F}\}$. In passing from $\mathcal{F}$ to $\mathcal{F}^+$, all re-entrant angles disappear.

[12] Strictly speaking, $\delta(\mathbf{C}_1, Z) = 1$ is found for *all* points $Z \in \mathbb{R}^2$. Therefore, the barycentre results from equations (2.13),(2.14) only for integration/summation over all $Z \in \mathcal{F}$.

C_{1v} symmetry are given in Table 2. Of course, in these figures all symmetry centroids lie on the mirror line, but they do not coincide. The data of Table 2 show a monotonous sequence of the symmetry centroids for increasing n only for the arrowhead figure $\mathcal{A}r$, whereas for the other figures—also for simple isosceles triangles (figures $\mathcal{T}ia$, $\mathcal{T}io$)—the convergence to the circularity centroid is not monotonous.

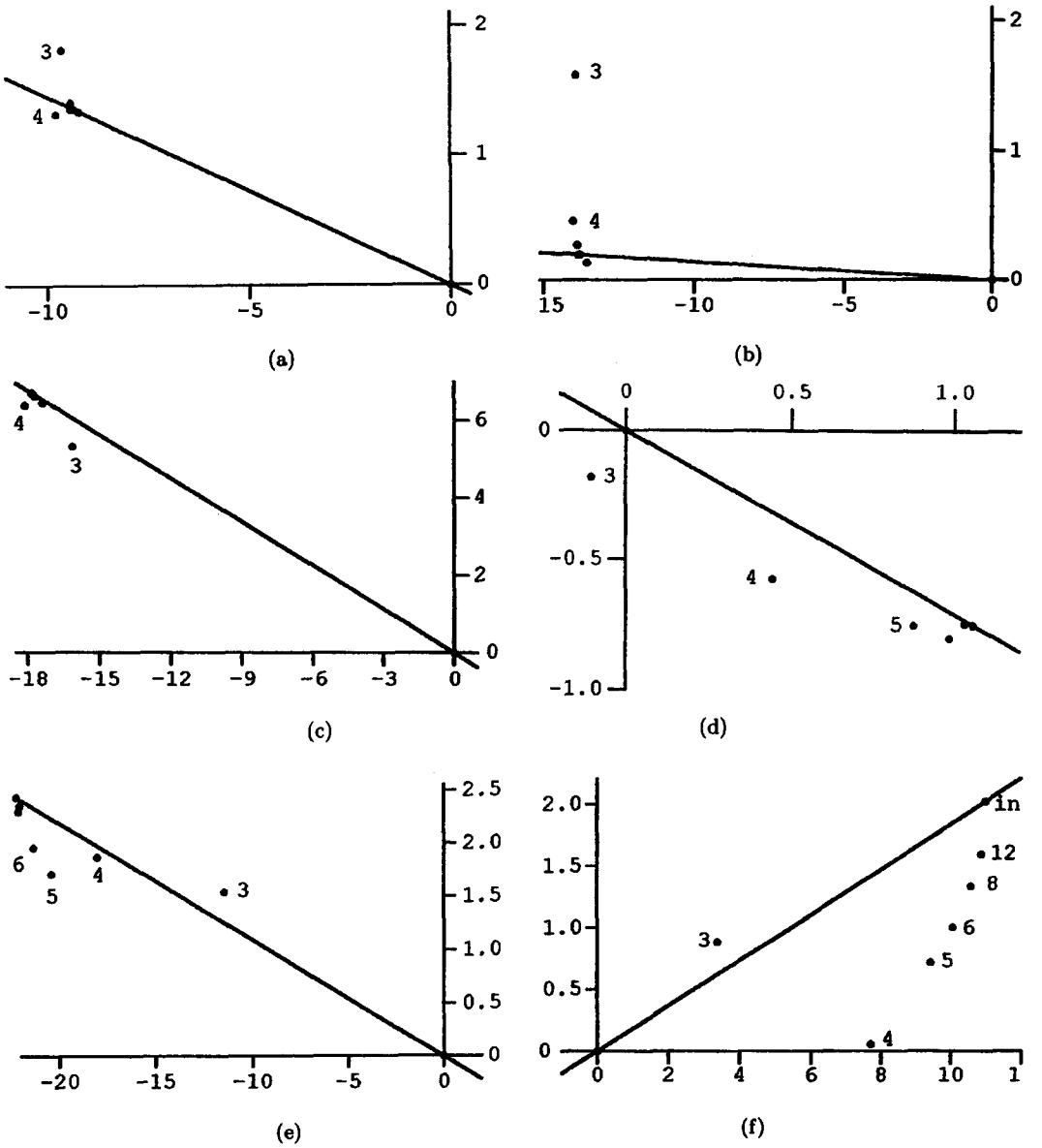

Figure 18. Positions of different polymetry centroids (multiplicity values are indicated) within the figures $\mathcal{T}r1$ (a), $\mathcal{T}r2$ (b), $\mathcal{Q}c$ (c), $\mathcal{H}i$ (d), $\mathcal{H}v$ (e), and $\mathcal{P}v$ (f). In all cases, the line connecting the barycentre B and the circularity centroid is plotted, and for (a)–(c) also the BW line (W: incentre) which coincides with the former line. Dimetry centroids coincide in all cases with the barycentre (origin).

Positions of the polymetry centroids in figures having C_1 symmetry are displayed in Figure 18. The most prominent feature of these diagrams is that the symmetry centroids of a figure lie near a straight line. For triangles ($\mathcal{T}r1$, $\mathcal{T}r2$, $\mathcal{T}o$) this is *not* the Euler straight line (the line connecting the barycentre, the orthocentre and the circumcentre of the triangle [7, Volume 3, p. 431]), but a straight line connecting the barycentre with the incentre (the intersection point of the angle bisectors) which is the point of maximum circularity for the triangle. In Figures 18a

and 18b, both the line connecting the barycentre B with the circularity centroid and the straight line intersecting the barycentre and the incentre W (outside the diagrams) are plotted: they are identical. This means that the circularity centroid lies exactly on the straight line between the barycentre (the monometry centroid) and the incentre (the point of maximum circularity). Thus, the part $\mathcal{F} \setminus C$ (C: solid incircle) of the triangle $\mathcal{F}$ induces a shift of the circularity centroid away from the incentre, but in every case investigated here, this shift is along the BW line. On the other hand, the deviation of the trimetry centroid from the BW line is *significant* for all triangles (see especially Figure 18b), so that this line can be regarded only as an *approximate* locus of the symmetry centroids of a triangle.

The same is true for the circumscribed quadrangle $\mathcal{Q}c$ (Figure 18c). This figure also possesses an incircle, and the circularity centroid lies exactly on the BW line. The symmetry centroids cluster around the circularity centroid with the exception of the trimetry centroid which lies, however, near the BW line.

The irregular quadrangles $\mathcal{Q}u1$ and $\mathcal{Q}u2$ (not shown) also have their symmetry centroids arranged near straight lines with surprisingly small deviations from these lines. Roughly, we find that the symmetry centroids lie the more closely to a straight line the higher the degree of symmetry of the figure with respect to this line. For $\mathcal{T}ia$, $\mathcal{T}io$, $\mathcal{A}r$, and $\mathcal{D}e$ (Table 2), this line is a crisp mirror line for the figures.

In $\mathcal{Q}u2$, the trimetry centroid lies less than halfway between the barycentre and the circularity centroid, but all other symmetry centroids cluster near the latter. For other irregular figures (for example, $\mathcal{H}i$, $\mathcal{H}v$, $\mathcal{P}v$), the clustering of the symmetry centroids around the circularity centroids breaks down completely. This effect is equally strongly pronounced in convex ($\mathcal{H}i$) and concave ($\mathcal{H}v$, $\mathcal{P}v$) figures. These findings resemble those for figures with $\mathbf{C}_{1v}$ symmetry (see Table 2), especially figure $\mathcal{A}r$.

From the symmetry centroids of convex figures also, the special role of $\mathbf{C}_2$ (but also $\mathbf{C}_1$) is evident. Whereas centroids for $\mathbf{C}_3$ and higher rotation symmetries are often lumped near the $\mathbf{C}_{\infty v}$ centroid and converge to it for increasing n, the $\mathbf{C}_2$ centroid (in all cases investigated so far) coincides within the margins of error with the barycentre of the figure (the $\mathbf{C}_1$ centroid).

3. DISCUSSION AND CONCLUSIONS

An important advantage of the fuzzy symmetry concept is the possibility of a *separate* characterisation of the $\mathbf{C}_n$ and $\mathbf{C}_{nv}$ symmetries of planar figures. Therefore, a remark on the nomenclature of these symmetry aspects seems to be in order. Table 3 gives a compilation of some customary denominations.

Table 3. Some common terms for $\mathbf{C}_n$ and $\mathbf{C}_{nv}$ symmetry-related notions.

n	$\mathbf{C}_n$-symmetric [12]	$\mathbf{C}_n$-symmetric [5]	$\mathbf{C}_{nv}$-symmetric [5]	$\mathbf{C}_{nv}$-symmetry [11]
1	monogyric	monometric	monosymmetric	—
2	digyric	dimetric	disymmetric	elongation
3	trigyric	trimetric	trisymmetric	triangularity
4	tetragyric	tetrametric	tetrasymmetric	squareness
5	pentagyric	pentametric	pentasymmetric	—
6	hexagyric	hexametric	hexasymmetric	—
...	...	...	...	...

Bird *et al.* [11], for example, use a mixture of different notions for $\mathbf{C}_{nv}$ symmetry.[13] Out of these, "triangularity" has been used in the title of this paper because of its pictorial quality.

[13]The statement made in [11] that the Fourier term F_k for $k = 2, 3, 4, \ldots$, describes the elongation, triangularity, squareness, etc., of a figure is *not* correct. As has been outlined in [1], *all Fourier terms which are compatible* with the symmetry tested (i.e., all terms whose index k is a multiple of the multiplicity tested) contribute to the degree of rotational symmetry. In particular, it is possible to have a degree of $\mathbf{C}_{nv}$ symmetry up to unity, even if the term F_n is completely absent.

Since, however, polygons are given Latin names only for $n = 3, 4$, for the sake of uniformity of the nomenclature, the Greek-derived terms "*polymetry*" and "*polysymmetry*" have been preferred[14] (for example, the term "quinquangularity" seems not to become generally accepted despite Mackay's fine article *"De nive quinquangula"* [13]), especially since this nomenclature is used in crystallography [5], and partially in biology. Standard books like [14–16] use the terms "monosymmetric", "disymmetric", etc., for the description of $\mathbf{C}_{nv}$ symmetry in botanical objects, and also the notion "polysymmetry" is used for $\mathbf{C}_{nv}$ ($n > 2$) symmetry [14–16]. The term "circularity" has been introduced here instead of coining new terms like "apeirometry" and "apeirosymmetry" for infinitefold axes ('$\acute{\alpha}\pi\varepsilon\iota\rho o\varsigma$: infinite).

The method for the determination of *symmetry regions* presented here shows that in a figure $\mathcal{F}$ (for all positions $Z \in \mathcal{F}$ of the rotation point), *all* $\mathbf{C}_n$ and $\mathbf{C}_{nv}$ symmetries can objectively be found. This means that for arbitrary plane point groups $\mathbf{G}$, regions in $\mathcal{F}$ (centering around Z) can be found that have the symmetry $\mathbf{G}$ to be tested. However, (analogous to the findings derived from the Fourier analysis), in many instances these symmetries are not present *per se*[15] (this would be forbidden because these symmetries are incompatible with the actual symmetry $\mathbf{G}_A$ of the figure), but as subgroup symmetries of symmetries which are supergroups of the actual symmetry $\mathbf{G}_A$ of $\mathcal{F}$. In any case, we may speak of the (degree of) triangularity of a square or even the (degree of) circularity of this figure. The latter is numerically given by the relative weight of the F_0 term in the Fourier analysis or, in the method presented here, by the relative area of the incircle of the square or, generally, the *maximal circle* about Z.

The symmetry regions within a geometric figure have also been found to sensitively reflect *local symmetries* which are not crisp symmetries of the whole figure. Such local symmetries enhance the symmetry of symmetry regions, most drastically seen with $\mathbf{C}_n$ regions. In sum, there are two possible reasons for finding higher symmetries than $\mathbf{C}_n$ in a polymetry region.

(i) The *site symmetry* of the rotation point Z is greater than $\mathbf{C}_n$. A closer inspection of the case that the symmetry tested corresponds to a $\mathbf{G}_A^{\neq}$ group and exists in $\mathcal{F}$ only as subgroup symmetry of a supergroup of the actual symmetry $\mathbf{G}_A$ shows that this is a special case. For the square discussed in Section 2.3, the site symmetry of Z is $\mathbf{C}_{4v}$, so that for the $\mathbf{C}_3$ region, we get $\mathrm{Gen}(\mathbf{G}(\mathcal{G}(\mathbf{C}_3))) = \mathrm{Gen}(\mathbf{C}_3) \cup \mathrm{Gen}(\mathbf{C}_{4v}) = \mathrm{Gen}(\mathbf{C}_{12v})$.

(ii) The rotation point Z lies on *local* symmetry elements which are not crisp symmetry elements of the whole figure.

By elucidating the reasons for the symmetries of symmetry regions within a geometric figure, such an examination can sharpen our awareness of fuzzy symmetries in such a figure.

Symmetry profiles and landscapes have already been determined by us in [6,17], but on the basis of a Fourier analysis of the figure's contour function $R(\varphi)$. A comparison (Figures 1c, 1d, 7a, and 7b) shows that these values may be very similar to those calculated with the method presented here (for the square), though data for a solid polygon and for its contour line may also differ considerably (e.g., for the rectangle). Our method shows that symmetry profiles and landscapes can extend beyond the rim of the figure if it is concave (it has re-entrant angles). This is an aspect that cannot be dealt with by simple Fourier analysis since, in this case, we are faced with multivalued contour functions.

A consistent further development from the symmetry landscapes is the determination of *symmetry centroids* for geometric figures which has been done here for the first time. That these centroids do not coincide in figures with low symmetry ($\mathbf{C}_{1v}$ or $\mathbf{C}_1$) could be expected from theoretical grounds, but here we are able to give numerical data for this phenomenon and posi-

[14]In the end, these terms do not optimally reflect the gist to be expressed by these denominations. However, the terms "polymetry" and "polysymmetry" are already in a certain use in contrast to words like "gyricity" ('η $\gamma\upsilon\rho\acute{\eta}$: axis) or "catoptricity" ($\tau\acute{o}$ $\kappa\acute{\alpha}\tau$-$o\pi\tau\rho o\nu$: mirror) though terms like "hexa*gyric*" or "pleur*optric* " have been used by Wolfand Wolff [12] in a somewhat different context.

[15]In our case, presence *per se* of a $\mathbf{C}_n$ symmetry means that we have regions $\mathcal{G}(n_{\max})$ whose orbits have a maximal multiplicity $n_{\max} = n$.

tions of the different centroids. In any case, the symmetry centroids obey the *symmetry principle* which is valid for the barycentre of a figure (cf., [18]). *If there exist symmetry elements in the figure $\mathcal{F}$ under study, the symmetry centroids of $\mathcal{F}$ lie on each of them.* This means that for higher symmetries ($n > 1$), the barycentre of a geometric figure can be regarded as its *point of highest symmetry*, since it coincides with all symmetry centroids as well. For low-symmetric figures ($n = 1$), this is no longer true since the different symmetry centroids fall apart.

REFERENCES

1. A.E. Köhler, A fuzzy symmetry concept for forms with imperfect symmetries, *Computers Math. Applic.* **22** (9), 35–50 (1991).
2. M. Klemm, *Symmetrien von Ornamenten und Kristallen*, p. 4f, Springer-Verlag, Berlin, (1982).
3. N.F.M. Henry and K. Lonsdale, Editors, *International Tables for X-Ray Crystallography, Volume 1: Symmetry Groups*, p. 23, Kynoch Press, Birmingham, (1965).
4. T. Hahn, Editor, *International Tables for Crystallography, Volume A: Space-Group Symmetry*, D. Reidel, Dordrecht, (1987).
5. G. Tschermak, *Lehrbuch der Mineralogie*, p. 49f, Alfred Hölder, Wien, (1921).
6. A.E. Köhler, Crisp and fuzzy motif and arrangement symmetries in composite geometric figures, *Computers Math. Applic.* **27** (11), 67–87 (1994).
7. M. Hazewinkel, Editor, *Encyclopedia of Mathematics*, Volume 1–9, Reidel: Kluwer Academic, Dordrecht, (1987).
8. G. James and R.C. James, Editors, *Mathematics Dictionary*, p. 295, Van Nostrand Reinhold, New York, (1976).
9. S. Wolfram, *Mathematica: A System for Doing Mathematics by Computer*, Addison-Wesley, Redwood City, CA, (1991).
10. H. Burzlaff and H. Zimmermann, *Symmetrielehre*, p. 63, G. Thieme Verlag, Stuttgart, (1977).
11. J.L. Bird, D.T. Eppler and D.M. Checkley, Jr., Comparisons of herring otoliths using Fourier series shape analysis, *Can. J. Fisheries Aquat. Science* **43**, 1228–1234 (1986).
12. K.L. Wolf and R. Wolff, *Symmetrie*, p. 80, Böhlau Verlag, Münster, (1956).
13. A.L. Mackay, De nive quinquangula—o pyatiugol'nykh snezhnikakh, *Kristallografiya* **26**, 910–919 (1981); *Soviet Phys. Crystallogr.* **26**, 517–522 (1981).
14. K. Linsbauer, Editor, *C.K. Schneider's Illustriertes Handwörterbuch der Botanik*, p. 692, Wilhelm Engelmann, Leipzig, (1917).
15. P. Sitte, H. Ziegler, F. Ehrendorfer and A. Bresinsky, *Strasburger: Lehrbuch der Botanik für Hochschulen*, Gustav Fischer, Verlag, (1991).
16. F.W. Stöcker and G. Dietrich, Editors, *Brockhaus ABC Biologie*, Verlag, Leipzig, (1986).
17. A.E. Köhler, A second approach to fuzzy symmetries: Fuzzy symmetry requirements, *Computers Math. Applic.* **25** (1), 17–34 (1993).
18. McGraw-Hill Encyclopedia of Science and Technology, Volume 3, p. 422, McGraw-Hill, New York, (1992).